

Waves and Turbulence in the Very Local Interstellar Medium: From Macroscales to Microscales

Federico Fraternale on Nikolai V. Pogorelov 1,2 to

Center for Space Plasma and Aeronomic Research, University of Alabama in Huntsville, Huntsville, AL 35805, USA; federico.fraternale@uah.edu
Department of Space Science, University of Alabama in Huntsville, Huntsville, AL 35805, USA
Received 2020 August 30; revised 2020 October 28; accepted 2020 November 7; published 2021 January 11

Abstract

Voyager 1 (VI) has been exploring the heliospheric boundary layer in the very local interstellar medium (VLISM) since 2012 August. The measurements revealed a spectrum of fluctuations over a vast range of space and timescales, but the nature of these fluctuations continues to be an intriguing question. Numerous manifestations of turbulence cannot be explained using a single phenomenology. Weak shocks and compressions are the prominent features of the VLISM. We use high-resolution (48 s) measurements to perform a multiscale analysis of turbulence at VI between the years of 2013.36 and 2019.0 (124–144 au from the Sun). On relatively large scales, wave trains of mixed compressible/transverse nature with the correlation scale in the range of 15–100 days dominate the spectrum of fluctuations. The observed magnetic field profiles are suggestive of a Burgers-like (f^{-2}) turbulence phenomenology induced by solar activity. We demonstrate that the level of large-scale compressible fluctuations is still significant in late 2018. We analyze the turbulence down to small scales comparable to the ion inertial length and show that magnetic compressibility is always large on these scales. Besides the shock-induced turbulence measured from 2014.486, the intensity and intermittency of small-scale fluctuations have been growing smoothly since 2018.5. Our analysis suggests that local processes are contributing to the production of turbulence on small scales. We present the estimates of transport coefficients in the plasma traversed by VI. The range of scales is identified where VI measurements are affected by the contribution from pickup ions.

Unified Astronomy Thesaurus concepts: Interstellar magnetic fields (845); Heliopause (707); Heliosphere (711)

1. Introduction

Since crossing of the heliopause (HP) in 2012 August and 2018 November, respectively (Stone et al. 2013; Burlaga et al. 2019), Voyager 1 and 2 spacecraft (V1, V2) have been sampling the very local interstellar medium (VLISM) in situ. The term VLISM is used here as an identifier of the part of the local interstellar medium (LISM) region affected by the presence of the heliosphere. Note that this definition differs from the one used by, e.g., Holzer (1989) and Cairns & Zank (2002), where this term was applied to both perturbed and unperturbed LISM in the vicinity of the HP. Our definition generalizes the one in Zank (2015) by including the possibility of heliospheric effects on high-energy cosmic rays (Zhang et al. 2020) and considerably larger distances at which the heliosphere affects the LISM in the heliotail and Sun's polar directions (Pogorelov et al. 2017a). This definition of VLISM is frequently used interchangeably with the term outer heliosheath (Pogorelov et al. 2013; Gurnett et al. 2015; Burlaga et al. 2018). The heliospheric boundary layer (HBL) is the relatively narrow region of depressed plasma density on the interstellar side of the HP (Gurnett et al. 2015; Pogorelov et al. 2017b). The HBL is a subregion of the VLISM, where the interstellar magnetic field (ISMF) drapes around the HP, and electron plasma waves and 2-3 kHz radio emission has been observed (Burlaga & Ness 2014; Kim et al. 2017; Gurnett & Kurth 2019). While VLISM extends to a few hundred astronomical units in its upstream direction, the width of the HBL is of the order of the charge-exchange mean-free path in the VLISM, which is about 40-50 au. It is therefore not surprising that the HBL itself exists due to charge exchange (Baranov & Malama 1993) and disappears in magnetohydrodynamic (MHD) simulations involving the ISMF if the interstellar neutrals are ignored (Pogorelov & Matsuda 1998). Pickup ions (PUIs), which are produced in the process of charge exchange between ions and neutral atoms of both heliospheric and interstellar origin, Galactic cosmic rays (GCRs), and time-dependent solar activity together make the VLISM a dynamically complex region (see, e.g., Zank 2015; Pogorelov et al. 2017a).

Magnetic field fluctuations in the VLISM are observed across a vast range of scales (Burlaga et al. 2015, 2018; Fraternale et al. 2019a, 2020; Burlaga et al. 2020a). The largest fluctuations identified until now are associated with shock/compression waves traveling outward into the VLISM (Burlaga et al. 2013; Gurnett et al. 2013, 2015; Burlaga & Ness 2016; Burlaga et al. 2019). These shocks occur when pressure pulses, shocks, and other discontinuities, often related to global merged interaction regions (GMIRs) hit the HP from the inner heliosheath (IHS) side. They generate relatively large perturbations in the VLISM, as was suggested initially by Gurnett et al. (1993) and later demonstrated in numerous simulations (Steinolfson 1994; Pogorelov 1995, 2000; Zank & Müller 2003; Washimi et al. 2011; Borovikov et al. 2012; Pogorelov et al. 2013; Fermo et al. 2015; Kim et al. 2017; Matsukiyo et al. 2019).

Both the small-amplitude wave analysis of Zank et al. (2017) and numerical simulations of Matsukiyo et al. (2019) show that fluctuations carried by the solar wind (SW) are transmitted into the VLISM as fast-magnetosonic modes. This may explain a relatively high level of compressible turbulence identified by Burlaga et al. (2015) in the daily averaged VI data in the range of frequencies $2.5 \times 10^{-8} < f < 1.15$ Hz. Burlaga et al. (2018) also investigated the VLISM turbulence in the interval of the years 2015–2016 and showed that Alfvénic fluctuations become dominant in the same range of frequencies. Zank et al. (2019)

suggested that a possible mechanism for the generation of transverse fluctuation is the decay of fast modes into transverse modes via three-wave nonlinear interaction. Initially, small-scale fluctuations were not considered because of the high level of noise and abundance of data gaps in the Voyager time series. Fraternale et al. (2019a) was the first to perform a spectral and intermittency analysis of high-resolution (48 s) VI data in the frequency range of $10^{-8} < f < 10^{-2}$ Hz. Recently, Fraternale et al. (2020) have demonstrated the presence of physically meaningful fine-scale turbulence ($10^{-4} < f < 10^{-2}$ Hz, $1 \lesssim \ell \lesssim 100$ ion inertial lengths) with filamentary structures revealing themselves in front of and behind the shock that overtook VI in 2014.65. Such a region of enhanced turbulence is associated with the plasma wave event and recovery of the GCR flux perpendicular to the ISMF (Gurnett et al. 2015; Rankin et al. 2019). The presence of a spectral break at 10^{-4} Hz led us to the conclusion that local processes can affect small-scale turbulence in the VLISM.

In this paper, we discuss typical scales and parameters of the VLISM plasma, including the transport coefficient derived from the theory of Coulomb collisions. We investigate magnetic field distributions and analyze the spectrum and high-order moments of magnetic field fluctuations observed in situ by V1 from 2013.36–2019.0. We demonstrate that largescale turbulence is not homogeneous in the considered time intervals. It often contains coherent waveforms that seem to experience nonlinear steepening, as suggested by the presence of N-shaped profiles both in observations and numerical models (Kim et al. 2017; Matsukiyo et al. 2019). Such quasiperiodic structures reveal themselves on correlation scales that are be related to solar rotation, and were observed throughout the year of 2019. This suggests that the pristine interstellar turbulence is not yet observed due to the continuous heliospheric forcing. This conclusion is also consistent with the recent analysis of the Interstellar Boundary Explorer (IBEX) observations, which speaks in favor of the local origin of observed turbulence (Zirnstein et al. 2020). The observed Fourier spectra in the large-scale regime often display a -2spectral index, which may be indicative of the Burgers-like phenomenology rather than the Kolmogorov scenario. As far as the small-scale regime is concerned, besides the 2014 shockrelated event, we also demonstrate the presence of relatively intense intermittent structures in 2018–2019. Despite the noise and data errors clearly affecting this regime, we maintain that those intermittent structures, as well as high level of magnetic compressibility and clear correlations between the magnetic field components, are not typical of purely noise signals. In addition, we demonstrate that the self-generated turbulence due to the instabilities of the PUI distribution (Roytershteyn et al. 2019) may also occur in this range of frequencies.

The paper is structured as follows. In Section 2, we describe the data sets chosen for our analysis. In Section 3, we present an overview of plasma distributions and magnetic field structures observed in the HBL throughout the year of 2019. In Section 4, we analyze the spectral properties of magnetic field fluctuations. In particular, Section 4.1 discusses the applicability of Taylor's approximation. In Sections 4.2 and 4.3, we present the power spectra in the low- and high-frequency ranges. In Section 4.4, we analyze the intermittency and third-order magnetic moments of Voyager data revealing the nature of turbulent VLISM plasma. A summary and discussion are presented in Section 5. In Appendix A, we report details in the

calculation of collisional transport coefficients, and in Appendix B we estimate the convergence and accuracy of high-order statistics.

2. V1 Data Sets

We analyze magnetic field distributions measured by V1 in five distinct time intervals chosen between the years of 2013.36 and 2019.0, at heliocentric distances ranging between 126 and 142 au. We use the 48 s resolution data, which is the highest resolution publicly available at the NASA Space Physics Data Facility (https://cohoweb.gsfc.nasa.gov/coho/). Data are provided in the spacecraft-centered (RTN) coordinate system. The R-axis is directed radially outward from the Sun, the T-axis is parallel to the Sun's equatorial plane and oriented in the direction of the Sun's rotation, while the N-axis completes the right coordinate system. In this study, it was convenient to rotate the data to the principal-axis reference frame, which is defined as follows. The first axis (the ||-axis) is aligned with the principal direction of the magnetic field B, defined as the principal axis of the ellipsoid, which provides us with the best fit of the data. Its positive direction coincides with the positive direction of the T-axis. The corresponding unit vector, $\hat{\boldsymbol{e}}_{\parallel}$, is the eigenvector related to the largest eigenvalue of the correlation tensor

$$S = \begin{bmatrix} \langle B_R^2 \rangle & \langle B_R B_T \rangle & \langle B_R B_N \rangle \\ \langle B_T B_R \rangle & \langle B_T^2 \rangle & \langle B_T B_N \rangle \\ \langle B_N B_R \rangle & \langle B_N B_T \rangle & \langle B_N^2 \rangle \end{bmatrix}, \tag{1}$$

where the angular brackets stand for the ensemble average over the the data set points. The \perp_2 axis is orthogonal to the plane containing \hat{e}_{\parallel} and \hat{e}_N , i.e., $\hat{e}_{\perp 2} = \hat{e}_{\parallel} \times \hat{e}_N$, and is close to the radial direction. The third axis (\perp_1) completes the right-hand triplet and lies in the plane containing \hat{e}_{\parallel} and the *N*-axis. We occasionally perform a minimum-variance analysis. In this case, the unit vectors in the maximum-, intermediate-, and minimum-variance directions are referred to as \hat{e}_{\max} , \hat{e}_{int} , and \hat{e}_{\min} , respectively. They are determined by the eigenvectors of the variance ellipsoid for a specific data set. Hereinafter, the term "parallel" (or "longitudinal") refers to directions parallel to the average magnetic field vector. The term "perpendicular" (or "transverse") refers to directions perpendicular to the average magnetic field. The same notation will be used for the vector components.

Voyager data are affected by a relatively high noise. This is due to statistical and systematic errors of different origin, including those due to the calibration process (see details in Berdichevsky 2009; Burlaga et al. 2015). In the VLISM region sampled so far by V1, the 1σ uncertainty is estimated to be around $\pm 0.02 \,\mathrm{nT}$ for B_T and B_N , and higher for B_R $(\sim \pm 0.06 \, \mathrm{nT})$. The noise level related to the highest resolution of the low-field magnetometer is about $\pm 0.005\,\mathrm{nT}$. The interpretation of observational data in the VLISM requires caution, since most of fluctuations fall into the noise bin, especially for fluctuations of B_R . In addition to statistical noise, systematic jumps can be found in the data. Besides, the telemetry coverage is limited, which constitutes a major issue for a multiscale analysis. In particular, the presence of data gaps lasting for several hours per day, both in the IHS and HBL, makes it challenging to recover the spectral features in

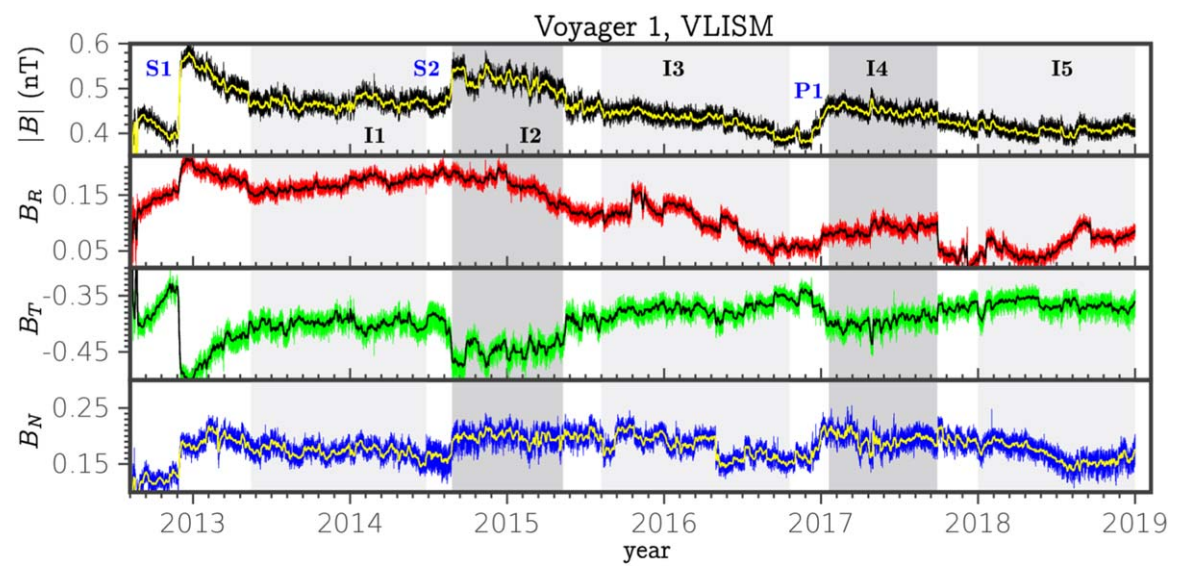


Figure 1. Magnetic field observed by VI in the VLISM. From top to bottom, the magnetic field magnitude and its R-, T-, and N-components are are shown. The thick lines show represent the field obtained with a 2-day running-average window. The shaded regions indicate the intervals selected for our analysis.

the frequency interval [10⁻⁵, 10⁻⁴] Hz (frequencies are measured in the spacecraft frame). We addressed this issue in our recent papers (Fraternale et al. 2019a, 2019b) by using different, independent spectral estimation techniques. In principle, it is necessary to estimate the influence of data gaps for each time interval considered. For the intervals analyzed here, the fraction of missing data is between 0.55 and 0.79.

Figure 1 shows the magnetic field magnitude and its R-, T-, and N-components in the VLISM sampled by V1 until 2019.0. The shaded intervals highlight the selected data sets, hereinafter referred to as I1-I5: day of year (DOY) 131-176, 2013 (I1), DOY 184, 2014—DOY 131, 2015 (I2), DOY 220, 2015— DOY 294, 2016 (I3), DOY 16-272, 2017 (I4), and DOY 1-365, 2018 (I5). Intervals I1 and I3 include weaker magnetic fields corresponding to the more rarefied plasma regions between shocks and/or compression waves. Note that the preshock interval lasting from 2014.486–2014.65 (the shock front) is not included in I1. That interval was analyzed in our previous paper (Fraternale et al. 2020). Magnetic turbulence analysis of daily data in similar intervals (up to the year of 2016) have been conducted by Burlaga et al. (2015, 2018). Interval I2 includes the compressed field in the region downstream of the shock wave, which overtook V1 on DOY 236, 2014. This shock is hereinafter referred to as S2. The previous shock (S1) overtook V1 in 2012.92. A detailed description of the magnetic field behavior up to the year of 2016 has been given by Burlaga & Ness (2016). Fraternale et al. (2019a) analyzed the properties of turbulence in 48 s averaged V1 data in the time intervals that included two compressed and two rarefied regions. Intervals I1-I3 in this paper correspond to intervals L2-L4 in our previous study.

Interval I4 includes the compressed field behind the large compression wave, which may, in principle, be interpreted as two shocks following each other and overtaking VI in 2016.94 (hereinafter referred to as P1). The accuracy of measurements does not allow us to make a conclusive statement regarding this. As described by Burlaga et al. (2019), interval I4 contains physically significant quasiperiodic oscillations whose origin is still unknown (Figure 2(b)). The end of interval I4 coincides with the sudden decrease of |B| observed in 2017.744. The

latter decrease lasted no more than ≈ 13 hr and included a data gap. During the subsequent time interval that lasted until 2018.0, another waveform of essentially transverse nature was detected (Figure 2(c)).

Interval I5 starts from the year 2018 to exclude some jumps in B_R , which still lack interpretation and may be due systematic errors. To our knowledge, no previous analysis of magnetic field turbulence from high-resolution data has been conducted so far in intervals I4 and I5. Burlaga et al. (2020a) showed the presence of transverse fluctuations between 2018.2 and 2019.49 in daily averaged data.

Table 1 summarizes the parameters of HBL plasma. Since the Plasma Science Subsystem onboard V1 stopped working in 1980, the plasma quantities need to be estimated. Information about the number density $n \approx n_e \approx n_p$ was indirectly derived by Gurnett et al. (2013, 2015) and Gurnett & Kurth (2019) from the electron plasma frequency f_{pe} of oscillations detected by the Plasma Wave Subsystem (see Figure 3 in Gurnett & Kurth 2019). The reported values of plasma temperature $T \approx T_p \approx T_e$ and the radial bulk flow speed can be derived from the simulation of Kim et al. (2017) by taking averages over the corresponding time intervals along the V1 trajectory. The simulated temperature is in the range of 25,000–35,000 K, and includes the effects of PUIs (see, e.g., Malama et al. 2006). One can see that such values are in agreement with recent V2 measurements in the HBL (Richardson et al. 2019) and earlier simulations (Pogorelov et al. 2015, 2017b). The radial velocity of interstellar plasma is assumed to be $-12 \,\mathrm{km \ s^{-1}}$ (sunward) during "quiet" intervals I1 and I3, and $-7 \,\mathrm{km \ s}^{-1}$ in the interval of compressed ISMF. The definitions of all quantities are given in the caption of Table 1 and in Appendix A.

3. Magnetic Field Structures in the VLISM

The ISMF in the VLISM is affected by the presence of the heliosphere. Perturbations, e.g., shocks and GMIRs traveling through the IHS eventually collide with the HP, and create shocks and compression waves in the VLISM. Among small-amplitude waves, predominantly fast-magnetosonic waves are transmitted across the HP (Zank et al. 2017; Matsukiyo et al. 2019). These compressible waves travel radially outward (anti-sunward) and are

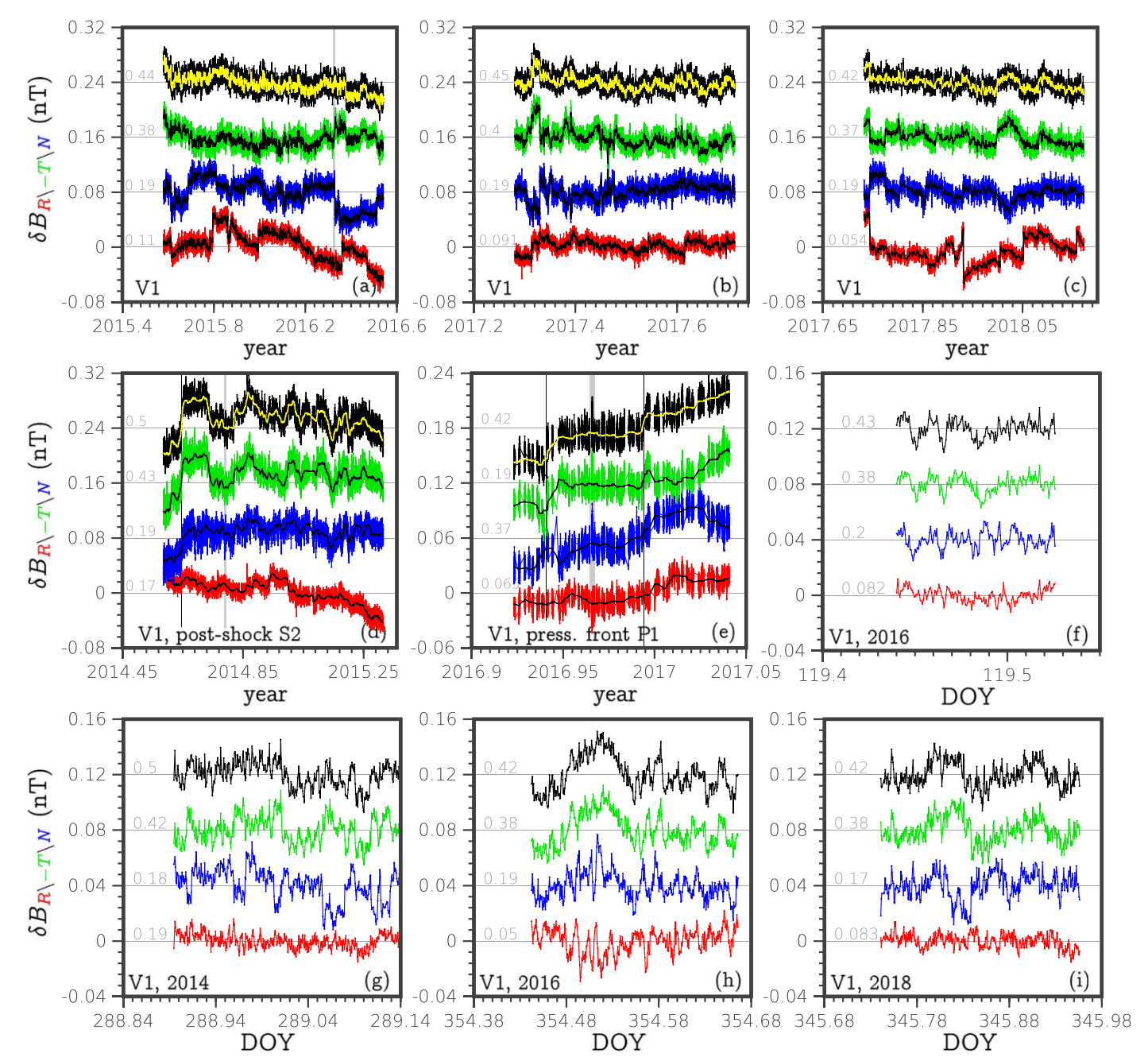


Figure 2. Magnetic field fluctuations detected by VI in the VLISM. Each panel displays the magnetic field components in the RTN frame shifted vertically for clarity. The red, green, and blue curves show δB_R , δB_T , and δB_N , respectively. Black curves show the field magnitude. Note that δB_T is shown with the opposite sign, for convenience. Panels (a), (b), and (c) show the coherent structures and wave trains with relatively large scale. Panel (d) shows the front of S2 and oscillations in the downstream region. Panel (e) presents a zoom-in of the 2017 pressure front, P1. Panels (f)–(i) show fine-scale structures obtained from data samples lasting a few hours. The gray bands in (a), (d), and (e) are magnified in panels (f), (g), and (h), respectively.

expected to steepen while interacting with the upstream turbulent medium. Shocks and compressions may catch each other (Kim et al. 2017) and generate other structures deeper in the LISM. The MHD theory (Kulikovskiy & Liubimov 1965) predicts that interaction of fast-mode compressible waves can generate other types of waves, including transverse (Alfvénic) waves. This phenomenon in the LISM has been studied by Zank et al. (2019). Besides, shock-related kinetic effects can affect the microscale turbulence, as shown recently by Fraternale et al. (2020). As a result, the VLISM sampled so far by *VI* exhibits both random and coherent structures on a vast range of spatial and temporal scales.

Figure 2 shows more detailed distributions of magnetic field fluctuations. The top panels show the presence of wave-train–like structures. Panel (a) shows a portion of I3 where large-scale fluctuations are predominantly transverse, as was first noted by Burlaga et al. (2018). One can see a clearly defined structure lasting \sim 100 days. There are three sharp jumps in B_R , which occurred at 2015.7955, 2015.9956, and 2016.3609, their amplitude being \sim 0.045 nT. A closer look at 48 s data shows that the first of these variations occurs smoothly within \sim 340 s and is related to rotation of B by \sim 6° about the local minimum-variance axis, which is oriented along $\hat{e}_{min} \approx (-0.12, 0.38, 0.92)$ (in the RTN

 Table 1

 Parameters of the Plasma in the Considered Time Intervals

Quantity	I1	I2	I3	I4	I5
Time interval	2013.37-2014.48	2014.66-2015.36	2015.60-2016.80	2017.05-2017.74	2018.0-2019.0
$d_{SC}(au)$	126.10 ± 2	130.14 ± 1.4	134.03 ± 1.9	138.50 ± 1.4	142.43 ± 1.9
B(nT)	0.466	0.516	0.434	0.450	0.408
$U_R(\text{km s}^{-1})$	-12	-7	-12	-7	-12
$n(\text{cm}^{-3})$	0.085	0.10	0.11	0.12	0.12
T(K)	3.0×10^{4}	3.4×10^4	2.6×10^{4}	2.7×10^{4}	2.5×10^{4}
$C_{\rm A}({\rm km~s}^{-1})$	34.8	35.9	28.2	27.0	25.6
$C_s(\text{km s}^{-1})$	28.7	30.5	26.7	27.2	26.2
$C_f(\text{km s}^{-1})$	45.1	47.1	38.9	38.4	36.7
$v_{th,p}(\text{km s}^{-1})$	22.2	23.7	20.7	21.1	20.3
$v_{th,e}(\text{km s}^{-1})$	954	1015	888	905	870
β	0.81	0.87	1.05	1.21	1.53
$r_{ip}(km)$	780	719	685	656	656
$r_{cp}(km)$	352	336	355	362	366
$f_{pe}(kHz)$	2.62	2.84	2.98	3.11	3.11
$f_{cp}(Hz)$	7.1×10^{-3}	7.9×10^{-3}	6.5×10^{-3}	6.6×10^{-3}	6.2×10^{-3}
$f_{cp,SC}(Hz)$	1.3×10^{-2}	1.1×10^{2}	1.3×10^{-2}	1.0×10^{-2}	1.2×10^{-2}
$f_{ip,SC}(Hz)$	5.9×10^{-3}	5.3×10^{-3}	6.7×10^{-3}	5.8×10^{-3}	7.0×10^{-3}
$f_{\text{PUI1,SC}}(\text{Hz})$	5×10^{-4}	4.7×10^{-4}	4.7×10^{-4}	4.0×10^{-4}	4.5×10^{-4}
$f_{\text{PUI2,SC}}(\text{Hz})$	2×10^{-3}	1.9×10^{-3}	1.9×10^{-3}	1.6×10^{-3}	1.8×10^{-3}
$f_{\rm PUI3,SC}({\rm Hz})$	8×10^{-3}	7.6×10^{-3}	7.6×10^{-3}	6.2×10^{-3}	7.2×10^{-3}
$\nu_s^{pp}(Hz)$	3.6×10^{-8}	3.5×10^{-8}	5.7×10^{-8}	5.9×10^{-8}	6.60×10^{-8}
$\nu_s^{ee}(\mathrm{Hz})$	1.6×10^{-6}	1.6×10^{-6}	2.5×10^{-6}	2.62×10^{-6}	2.92×10^{-6}
$\nu_s^{ep}(Hz)$	1.5×10^{-6}	1.51×10^{-6}	2.4×10^{-6}	2.5×10^{-6}	2.8×10^{-6}
$\nu_s^{pe}(\mathrm{Hz})$	8.4×10^{-10}	8.2×10^{-10}	1.3×10^{-9}	1.4×10^{-9}	1.5×10^{-9}
$\lambda^{pp}(au)$	4.10	4.45	2.4	2.4	2.1
λ^{ee} (au)	3.95	4.29	2.3	2.3	2.0
$\sigma(S/m)$	1.50×10^{3}	1.78×10^{3}	1.22×10^{3}	1.30×10^{3}	1.15×10^{3}
$\eta(\Omega \mathbf{m})$	6.7×10^{-4}	5.6×10^{-4}	8.2×10^{-4}	7.8×10^{-4}	8.7×10^{-4}
μ_0^p (Pa s)	1.2×10^{-6}	1.27×10^{-6}	6.62×10^{-7}	7.23×10^{-7}	6.0×10^{-7}
μ_0^e (Pa s)	9.4×10^{-7}	2.15×10^{-8}	1.33×10^{-8}	1.24×10^{-8}	1.0×10^{-8}
$D_{\mu}(\text{m}^2 \text{ s}^{-1})$	6.7×10^{15}	7.66×10^{15}	3.60×10^{15}	3.62×10^{15}	3.00×10^{15}
$D_n(\text{m}^2 \text{ s}^{-1})$	5.3×10^2	4.45×10^{2}	6.52×10^{2}	6.17×10^2	6.89×10^{2}
$D_{\text{Bohm}}(\text{m}^2\text{ s}^{-1})$	1.85×10^{3}	1.87×10^{3}	1.73×10^{3}	1.80×10^{3}	1.75×10^{3}
$D_{\text{th}}(\text{m}^2 \text{ s}^{-1})$	1.45×10^{16}	1.30×10^{16}	6.11×10^{15}	6.15×10^{15}	5.00×10^{15}

Note. Here $C_A = B_0/\sqrt{\mu_0 n m_p}$ is the Alfvén speed, $C_s = \sqrt{\gamma k_B (2T)/m_p}$ is the plasma sonic speed, $C_f = \sqrt{C_A^2 + C_s^2}$ is the (maximum) magnetosonic speed, $v_{th,p} = \sqrt{2k_BT/m_p}$ and $v_{th,e} = \sqrt{2k_BT/m_e}$ are the thermal speeds of protons and electrons, $\beta = nk_B (2T)/(B^2/2\mu_0 n_p m_p)$ is the plasma beta, r_{tp} and r_{cp} are the ion inertial length and the Larmor radius, $f_{pe} = \omega_{pe}/2\pi$ is the electron plasma frequency, f_{cp} is the gyrofrequency, $f_{cpSC} = |U_R - V_{SC}|/(2\pi r_{cp})$ and f_{tpSC} are the Doppler-shifted gyrofrequency and inertial scale, f_{PUIISC} , f_{PUIISC} , and f_{PUIISC} are the spacecraft-frame frequencies corresponding to the gyroscale of PUIs traveling at 400, 100, and 25 km s⁻¹, respectively, v_s^{pp} , v_s^{ee} , v_s^{ee} , v_s^{ee} , v_s^{ee} , v_s^{ee} , are the Coulomb-collision frequencies (see Equation (A4)), λ^{pp} and λ^{ee} are the mean-free paths (Equation (A9)), σ and η are the electric conductivity and resistivity (Equation (A10)), and μ^p and μ^e are the proton and electron parallel viscosities (Equation (A8)) due to Coulomb collisions. The parallel kinematic viscosity, the magnetic diffusivity, and ion thermal diffusivity are D_μ , $D_{\tau p}$ and D_{th} , respectively, and D_{th} is Bohm's diffusion coefficient (Equation (A11)).

coordinates). The second jump is interrupted by a data gap lasting a few hours. The third jump is also preceded by a data gap, but occurs smoothly within \sim 480 s. Here $\hat{\pmb{e}}_{min} \approx (-0.16, 0.67, 0.71)$.

Using the Alfvén velocity to estimate the wavelength of this structure and assuming the validity of Taylor's approximation (discussed in Section 4.1) one obtains $\ell \approx C_A \tau \approx 1.6$ au. Note also that plasma oscillation events have been detected during time intervals ~2015.7–2015.85 and ~2016.6–2016.75 (Pogorelov et al. 2017a; Gurnett & Kurth 2019). A minimum in the GCR intensity caused by the pitch angle anisotropy was detected around 2016.0 (Rankin et al. 2019).

Panel (b) of Figure 2 shows a quasiperiodic wave train in interval I4. It has a mixed, compressible/transverse nature with $\hat{e}_{\rm max}\approx (-0.05,\,0.78,\,0.62)$. Its main periodicity in the spacecraft frame is $\tau\approx 25$ days ($f_{\rm SC}\approx 5.3\times 10^{-7}$ Hz). Some modulation with $\tau\approx 6$ days is also present in both B_T and B_N just downstream of the wave front (2017.3299–2017.38), which shows N-shaped profiles, which begin with steep jumps in both components. This provides us with a good example of fluctuations of two highly correlated components of B, regardless of the oscillation intensity being close to the noise threshold.

Since the magnetometers' sensors at the Voyagers are independent (Berdichevsky 2009), the presence of such correlations

 Table 2

 Fluctuation Parameters and Dimensionless Quantities

Quantity	Unit	I1	I2	I3	I4	I5
$\delta B_{\parallel,\mathrm{rms}}$	nT	0.0115	0.0145	0.0108	0.0100	0.0106
$\delta B_{\rm rms} = \langle \delta \mathbf{B} ^2 \rangle^{1/2}$	nT	0.0164	0.0205	0.0260	0.0197	0.0230
$\delta b_{\rm rms} = \langle \delta \boldsymbol{b} ^2 \rangle^{1/2}$	$km s^{-1}$	1.23	1.41	1.70	1.24	1.45
$\ell_c = \int E_m(f) f^{-1} df / \int E_m(f) df$	au\days	1.06\63.5	0.26\19	1.26\76	0.26\19	0.98\60
$\ell_T = \left[-\frac{1}{2} \rho''(0) \right]^{-1/2}$	(km\hr)	5000\0.048	5200\0.06	7400\0.07	4700\0.054	6500\0.063
$Re = (U_{\rm ref} {\rm L}_{\rm ref})/D_{\mu}$		58	57	120	120	143
$Re_m = (U_{\text{ref}}L_{\text{ref}})/D_{\eta}$		7.0×10^{14}	8.4×10^{14}	5.7×10^{14}	6.1×10^{14}	5.4×10^{14}
$Re_{m,\text{eff}} = \left(\lambda_c/r_{ip}\right)^{4/3}$		1.2×10^{7}	0.2×10^{7}	1.8×10^{7}	0.2×10^{7}	1.4×10^{7}
$M_{ m turb} = \delta \ { m b}_{ m rms}/C_s$		0.042	0.046	0.063	0.046	0.055

Note. The quantities ℓ_c and ℓ_T are the integral scale computed from the power spectrum and magnetic Taylor microscale computed from the correlation functions (Equation (2)) using Richardson's extrapolation technique (see, e.g., Weygand et al. 2009).

serves as an important indicator for assessing whether the observed fluctuations represent real physical processes in the LISM plasma. Provided that this perturbation has a predominantly fast-mode character while overtaking VI, which traveled radially outwards in the wake of P1, the wavelength can be estimated as $\ell \approx (C_f - |U_R| - V_{\rm SC})\tau \approx 0.2$ au, where $V_{\rm SC} = 17~{\rm km~s^{-1}}$ is the spacecraft speed. Due to the Doppler shift, the actual wave period of the quasiperiodic perturbation shown in Figure 2(b) in the fixed frame, is $\sim 15~{\rm days}$. On the other hand, one might consider the possibility that the above perturbation was generated due to the interaction of compression wave P1 with preexisting upstream fluctuations. If the structure was advecting sunward, the wavelength would be approximately $\ell \approx (|U_R| + V_{SC})\tau \approx 0.35~{\rm au}$.

It is worth noting that both interpretations give essentially similar results. In reality, the actual direction and propagation velocity of these wave-like structures cannot be identified from the 1D data. No single-spacecraft measurements can provide us with such information, especially in the absence of plasma data. In this study, as described further in Section 4.1, we assume that a wavenumber anisotropy is present, so that the scale of gradients perpendicular to $\bf{\it B}$ are smaller than those parallel to $\bf{\it B}$, i.e., $k_\perp\gg k_\parallel$.

A clearly defined transverse wave followed by a more compressive waveform is shown in panel (c). N-shaped profiles of the period of \approx 20 days again are found in the B_N component. The scale of largest gradients in B_N is about 1 day ($\ell \approx 0.015$ au). The jumps in B_R that happened around 2017.93 and 2018.0518 might have been affected by systematic errors, as such transitions last 48 s, which would roughly correspond to a spatial thickness of \sim 2 r_{ip} . It is of interest, however, that these profiles are similar to those in panel (a).

Panel (d) shows the shock wave S2 (black vertical line) and its downstream region, which contains compressible fluctuations with the principal wave period of $\tau \sim 60$ days. A secondary wave period of \sim 24 days is also present. This interval was earlier discussed by Burlaga & Ness (2016). A detailed description of small-scale magnetic field fluctuations in front of and behind the shock is given in Fraternale et al. (2020). It is curious to see a similarity with the damped oscillations found downstream of supercritical shocks in the SW (see, e.g., Figure 1 in Saxena et al. 2005). However, the underlying physics is very different here. Our shock is subcritical ($M_f \approx 1.2$) and its VI passage time was $t_{\rm S2} \approx 3.3$ days. The estimated thickness is then $w_{\rm S2} \approx t_{\rm S2}(V_{\rm S2} - V_{\rm SC}) \approx 0.044$ au (\sim 10,000 r_{ip}), where $V_{\rm S2} \approx 40$ km s⁻¹ is the shock speed. For the 2012.92 shock (S1), Mostafavi & Zank (2018)

concluded that viscosity and thermal conduction due to Coulomb collisions are responsible for the observed thickness. Some questions regarding the shock structure are still open, we will address them in a separate study.

A decrease of magnetic field behind S2 cannot be attributed to ions trapped at the shock front on their gyration scale (the post-shock depression is ~ 0.7 au wide), so the nature of intense fluctuations in I2 remains uncertain. They may be of heliospheric origin, but a possibility exists that the downstream peaks are due to the interaction between S2 and upstream perturbations crossing the shock front.

As far as fast-mode shocks are concerned, incoming perturbations generate waves outgoing from the shock surface into the downstream region (McKenzie & Westphal 1970). Given the parameters shown in Table 1, this would mean sunward propagation, or a near-stationary state, in the fixed frame. The interaction would also modify the speed of the shock, as seen from numerical simulations of shock/turbulence interaction (Lele & Larsson 2009). In addition, the shock surface would also become corrugated. Fluctuations upstream of S2, if we assume that they are similar to those observed in interval I1, can be as intense as 0.04 nT, with typical wavelengths larger than the shock transition scale (see Figure 2 and Table 2). These large-scale magnetic pressure fluctuations ($\delta P_{\rm m} \sim 1.5 \times 10^{-14} \ {\rm Pa}$), are about 50% of the pressure jump associated with the shock ($\Delta P_{\rm m,S2}$). The rms of $|{\pmb B}|$ in II is 0.013 nT, and $\delta P_{\rm m,rms} \approx 3.7 \times 10^{-15} \ {\rm Pa} \approx 0.2 \ \Delta P_{\rm m,S2}$. In the Alfvén units $(\mathbf{b} = \mathbf{B}/\sqrt{\mu_0 m_p n_p})$, we obtain $\delta |\mathbf{b}|_{\text{rms}} \approx 0.9 \text{ km s}^{-1}$, which makes the turbulent Alfvén Mach number $M_{\rm A,turb} = \delta b_{\rm rms}/C_{\rm A}$ approximately equal to 0.027. It can become as high as 0.1 in the largest perturbations. This means that the instantaneous shock structure can vary significantly.

Another instance of possible large-scale wave interaction is shown in panel (e) of Figure 2. Here, we zoom into the pressure front P1. The overall front passed the spacecraft in $t_{\rm P1} \approx 35$ days. The corresponding thickness is $w_{\rm P1} \approx 0.26$ au, as estimated using the propagation speed $V_{\rm P1} \approx 30$ km s⁻¹ in the fixed frame (Kim et al. 2017). It is smaller than the propagation speed of S2, in accord with the decrease in temperature and increase in density with increasing heliocentric distance. Is should be noted that the overall width (from 2016.92–2017.05) of P1 is almost twice the thickness of S1, $w_{\rm S1} \approx 0.11$ au (the passage time of S1 was $t_{\rm S1} \approx 5.4$ days). Moreover, P1 has a two-step structure. The observation of two jumps marked with vertical black lines have been attributed to systematic errors in Burlaga et al. (2019).

Although the presence of two shocks following each other remains uncertain, one cannot exclude the possibility of that one shock (or a compression wave) is overtaking another. These shock interactions are abundant in numerical simulations (Kim et al. 2017). Clearly, one point per time measurement may easily miss this kind of interactions. It is worth noting that B_N shows a smoother profile, but still correlates with B_T , which may indicate that the two-step profile of P1 is a real feature and not an artifact.

Panels (f)–(i) of Figure 2 address small-scale fluctuations seen in data samples lasting a few hours with no gaps in the data. We show examples of relatively large fluctuations (sometimes above the noise threshold), for which the level of correlation among the components of \mathbf{B} is remarkable. In Fraternale et al. (2020), we provided a statistical analysis of enhanced fine-scale fluctuations and current sheets found in the regions in front of and behind S2, up to the year 2015. An example for such period is provided in panel (g). The scale of these fluctuations lies in the MHD-tokinetic transition regime. A typical passage time of the observed rapid shears at V1 is within a few 48 s intervals, which corresponds approximately to the spatial scale of \sim 5-20 r_{ip} . The normalized size is comparable to the typical thickness of current sheets and pressure-balanced structures found by Burlaga & Ness (2011) in the IHS, suggesting again that these may be real features intrinsic to the VLISM plasma. However, their origin should be attributed to local processes. In Fraternale et al. (2020), the turbulent, intermittent nature of this small-scale regime was also demonstrated (see the discussion in Section 4.3 and Section 4.4). Note that, as expected, small-scale intermittency is typically not observed in the VLISM, likely due to the level of noise. In this study, we also investigate the signatures of small-scale intermittency in the late 2018 data. The corresponding fluctuations are shown in panel (i). Table 1 summarizes the transport coefficients computed from the Coulomb-collision theory (see details in Appendix A). The mean-free paths $(\lambda^{pp,ee})$ associated with the Coulomb p-p and e-e collisions are computed using $T \approx 30,000 \,\mathrm{K}$. They are $\sim 4 \,\mathrm{au}$ in I1 and become smaller $(\approx 2.5 \text{ au})$ in I5. These values exceed those obtained by Mostafavi & Zank (2018) using the temperature of the unperturbed LISM equal to 7,500 K ($\lambda^{pp} \approx 0.3$ au). It should be reminded that the collision transport theory is applicable to magnetized plasma with $\omega_c/\nu \gg 1$ only when the macroscopic length scales in the directions parallel and perpendicular to \boldsymbol{B} satisfy the conditions $L_{\parallel} \gg \lambda$ and $L_{\perp} \gg \sqrt{\lambda r_c}$. For $\lambda^{ee} \approx 4$ au and $r_{ce} \approx 8$ km, one obtains $L_{\perp} \gg 7 \times 10^4$ km $\approx 100~r_{ip}$. For $\lambda^{pp} \approx 4$ au and $r_{cp} \approx 350$ km the condition becomes $L_{\perp} \gg 4 \times 10^5$ km $\approx 650~r_{ip}$. The mean-free path is larger than most of length scales in the spectrum of magnetic turbulence considered here (see Section 4). Since V1 moves approximately in the direction perpendicular to **B**, the constraint on L_{\perp} is satisfied for large-scale fluctuations, but not in small-scale regimes, where kinetic effects become important.

Information about the turbulence correlation scale is provided in Figure 3 for all intervals. We show the two-times correlation function of magnetic field fluctuations. The symmetric correlation tensor is defined by the formula

$$R_{ij}(\tau) = \frac{1}{2} \langle \delta B_i(t) \delta B_j(t+\tau) + \delta B_j(t) \delta B_i(t+\tau) \rangle, \quad (2)$$

where τ is the time lag measured at the spacecraft and angular brackets represent the time average. Panel (a) of Figure 3 shows the normalized trace of the correlation tensor (Equation (2)),

i.e., $\rho[B](\tau) = \sum_i^3 R_{ii}(\tau) / \sum_i^3 R_{ii}(0)$. Panel (b) shows the normalized autocorrelation of the field magnitude, denoted as $\rho[|B|] = \langle \delta |B|(t)\delta |B|(t+\tau) \rangle / \langle (\delta |B|)^2 \rangle$. The presence of quasiperiodic structures is evident from the analysis of the correlation function, which shows the presence of periodically occurring local maxima. This is an indicator of the heliospheric influence on the turbulence spectrum. The presence of large-scale transverse fluctuations can be inferred from the comparison of the two panels, and appears to be prominent in intervals I3 and I5. Larger scales in the system affected by the heliospheric activity correspond to the typical time interval between large shock waves, i.e., ~ 2 yr, or $\ell \sim 10$ au, in the VLISM observed so far by VI and, ultimately, to the ~ 11 yr solar cycle period.

The insert in panel (a) of Figure 3 shows a more detailed behavior of the correlation function for $\tau \in [0, 1800]$ s in the 48 s averaged data. It is worth noting that no sharp drop, which is expected at $\tau = 0$ in the presence of uncorrelated noise, is seen. This in agreement with our previous conclusions that high-resolution data contain information about physical processes occurring at small scales.

Magnetic field compressibility distribution for VLISM data during the period of 2013–2019 is shown in Figure 4. We use three estimators for the fraction of fluctuation energy in the direction of \boldsymbol{B} , i.e.,

$$C_1 = \left(\frac{\boldsymbol{B}_{<,\tau} \cdot \delta \boldsymbol{B}}{|\boldsymbol{B}_{<,\tau}||\delta \boldsymbol{B}|}\right)^2, \tag{3}$$

$$C_2 = \left(\frac{\delta |\mathbf{B}|}{|\delta \mathbf{B}|}\right)^2,\tag{4}$$

$$C_3 = \left(\frac{\boldsymbol{b}_{<,\tau} \cdot \delta \boldsymbol{B}}{|\delta \boldsymbol{B}|_{\text{rms}}}\right)^2, \tag{5}$$

where $B_{<,\tau}$ is the low-pass filtered field (running average) with the window τ , and the fluctuation is described by $\delta(\bullet) = (\bullet) - (\bullet)_{<,\tau}$. The mean-field unit vector is $\mathbf{b}_{<,\tau} = \mathbf{B}_{<,\tau}/|\mathbf{B}_{<,\tau}|$. Note that C_1 and C_2 are bounded in the interval [0,1] and give close results, while C_3 manifests the regions of most intense fluctuations parallel to **B**. It is therefore more spiky. In Figure 4, a 90 day window is chosen in the upper and middle panels to highlight the large-scale features in compressible fluctuations. Excluding period I4, it is in general true that after 2015 the level of magnetic compressibility decreases, on large scales, due to the presence of transverse fluctuations shown in Figures 1 and 2. The situation changes on small scales, as will be shown in Section 4 (see Figure 7). It is of interest, however, to note an increase in compressibility during the year of 2018, which is related to the presence of two pressure pulses occurring at 2018.386 and 2018.62.

4. Spectral Properties of Magnetic Field Fluctuations

VI 48 s data allow us to investigate spacecraft frequencies as high as 0.01 Hz. Since the ion gyroradii and inertial lengths are Doppler shifted to spacecraft frequencies $f_{\rm cp,SC}\approx 1.2\times 10^{-2}$ Hz and $f_{\rm i,SC}\approx 6\times 10^{-3}$ Hz, respectively, one can, in principle, observe the inertial, MHD regime of turbulence down to the MHD-to-kinetic transition. In Table 1, we show the Doppler

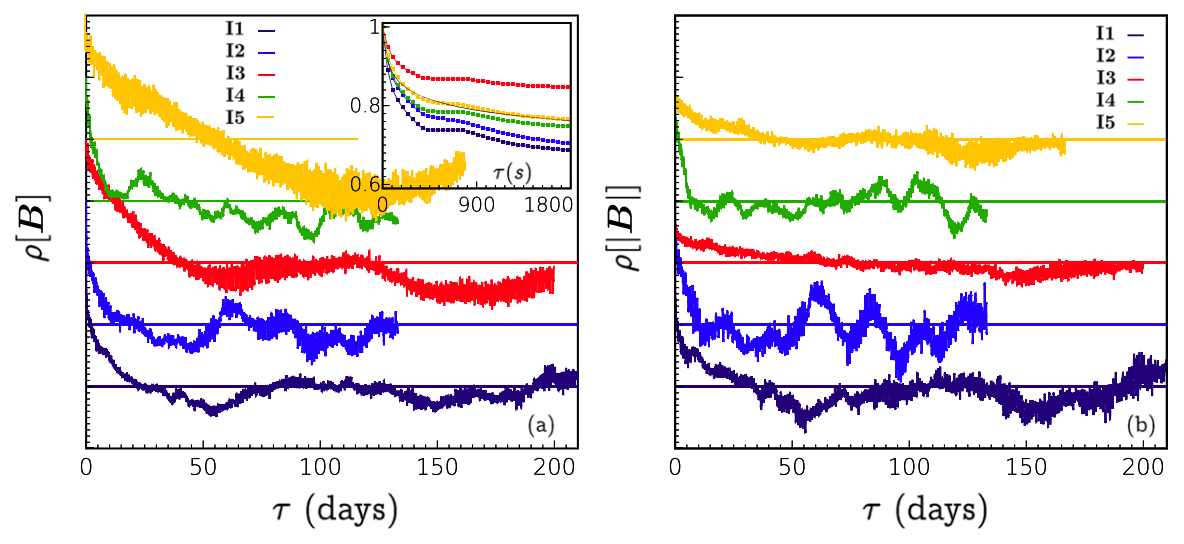


Figure 3. Normalized correlation functions. The trace of the symmetric correlation tensor (Equation (2)) (left panel) and autocorrelation of the magnetic field magnitude (right panel). The correlations are computed using 288 s averaged data, with no interpolation/reconstruction in the data gaps. Linear trends are removed from the data. The different color-coded curves represent the five intervals I1–I5, and are shifted by 0.5 for clarity. The horizontal lines represent the zero value for each curve. In the insert of panel (a), a magnification of the correlation function obtained from 48 s data is shown for $\tau \in [0, 1800]$ s. Here, the black curve shows the power-law fit for interval I5 ($\rho = 1.11 \ \tau^{-0.05}$).

shifted gyroradii of PUIs with speeds of 400, 100, and 25 km s⁻¹, respectively. The above values represent, respectively, the typical speeds of neutral atoms born in the supersonic SW, inner heliosheath, and interstellar medium. Such neutrals produce PUIs in the VLISM by charge-exchange processes. These fall into the frequency range of $4 \times 10^{-4} \lesssim f_{\rm SC} \lesssim 8 \times 10^{-3}$ Hz. Noise in the data, however, poses a challenge for interpretation of the high-frequency part of the observed spectrum, especially at $f_{\rm SC} \lesssim 10^{-4}$ Hz. Henceforth, we are introducing large ($f_{\rm SC} \lesssim 10^{-6}$ Hz), intermediate ($10^{-6} \lesssim f_{\rm SC} \lesssim 10^{-4}$ Hz), and small ($f_{\rm SC} \gtrsim 10^{-4}$ Hz) scales within the full observed spectral range. We will also imply small scales when talking about "microscale" regimes. In the horizontal axes used in Figures 5–7 have two distinct legends: one for the frequencies and the other one for perpendicular wavenumbers k_{\perp} , which are obtained using the Taylor hypothesis with $V_{\rm rel} = |U_R| + V_{\rm SC}$ (see Table 1 and further discussion in Section 4.1).

The reduced, 1D power spectral density of magnetic field fluctuations (PSD, or P) for intervals I1–I5 is shown in Figures 5 and 6. The Kolmogorov -5/3 scaling is shown as a reference slope. Figure 7 shows the spectral magnetic compressibility, defined as $C(f) = P[|B|]/E_m$, where $E_m = \sum_{j=1}^{3} P[B_j]$. In Table 2, we summarize the information about average fluctuation intensities, their integral scales, estimated Taylor's microscales, and Reynolds numbers.

4.1. Taylor's Hypothesis

Since spectral analyses are particularly insightful if expressed in terms of wavenumbers, here we discuss the applicability of Taylor's "frozen-turbulence" approximation in order to convert the frequencies measured by VI to wavenumbers. The Dopplershift relationship for a individual mode with wavenumber k reads as

$$\omega_{\rm SC}(\mathbf{k}) = \omega_{\rm PL}(\mathbf{k}) + \mathbf{k} \cdot \mathbf{V}_{\rm rel}(\mathbf{k}). \tag{6}$$

Here, the second term on the right-hand side is the Doppler shift calculated using the relative velocity $V_{\rm rel}=U-V_{\rm SC}$ (U is

the bulk velocity of plasma, $V_{SC} = (17 \text{ km s}^{-1}) e_R$ the spacecraft speed), $\omega_{\rm SC}=2\pi~{\rm f}_{\rm SC}$ is the angular frequency measured by the spacecraft, and ω_{PL} is the angular frequency in the plasma frame. In general, ω_{PL} includes the contribution of (i) nonlinear straining motions of turbulent eddies or wave structures, (ii) nondispersive MHD wave modes, and (iii) dispersive wave modes (typically relevant in the kinetic regime). In a scenario consisting of turbulent "eddies" with radius r, the nonlinear frequency for a generic scale $\ell=2\pi r$ can be expressed as $\omega_{nl}=2\pi/\tau_{nl}\sim 2\pi~\delta v/\ell\sim [k^3E(k)]^{1/2}$, where E(k) is the energy spectrum. For the Kolmogorov spectrum $E(k)=C_{\rm K}\epsilon^{2/3}k^{-5/3}$ (Kolmogorov 1941), the "turbulent" dispersion relation can be expressed as $\omega_{nl} \propto \epsilon^{1/3} k^{2/3}$ (in a reference frame moving with energy-containing eddies). This becomes $\omega_{nl} \propto \epsilon^{1/4} k^{3/4}$ in the assumption of the Iroshnikov-Kraichnan phenomenology (Iroshnikov 1964; Kraichnan 1965). For nondispersive wave modes, $\omega_{\rm PL}(\mathbf{k}) = \pm \mathbf{\textit{C}}_{\rm wave} \cdot \mathbf{\textit{k}}, \text{ where } \mathbf{\textit{C}}_{\rm wave} \text{ is the wave speed in the}$ plasma frame. The Taylor (1938) hypothesis allows for direct mapping of spacecraft frequencies into streamwise wavenumbers. This hypothesis holds provided that the Doppler shift (the last term in Equation (6)) for all modes is larger than the plasma frame frequency. At V1 in the VLISM, $V_{\rm rel} \approx 30 \, \rm km \ s^{-1}$. The upper bound for nonlinear frequency may be estimated as $\omega_{nl} < \delta v_{\rm max} k \approx \delta b_{\rm max} k \approx (3~{\rm km~s^{-1}})k$. Thus, it can be considered small $(\delta b_{\rm rms} \approx 0.9~{\rm km~s^{-1}})$. It is clear that Taylor's approximation can be violated because $V_{\rm rel}/C_{\rm A}\sim 1$, and also due to the possible presence of traveling compressible waves, which are expected especially near the HP.

However, it should be understood, first, that wavenumber anisotropy is likely to be present in magnetized plasmas. It is typical of the MHD turbulence, especially in the presence of strong mean fields, and at small scales down to the transitional/kinetic regime and results in $k_{\perp}\gg k_{\parallel}$ (e.g., Montgomery & Turner 1981; Goldreich & Sridhar 1995; Sahraoui et al. 2010), see also the review by Narita (2018) and references therein. For critically balanced fluctuations, it is possible that $k_{\perp}/k_{\parallel}\approx C_{\rm A}/\delta$ $v_{\rm rms}\approx 30~$ s, both the spacecraft velocity vector and bulk

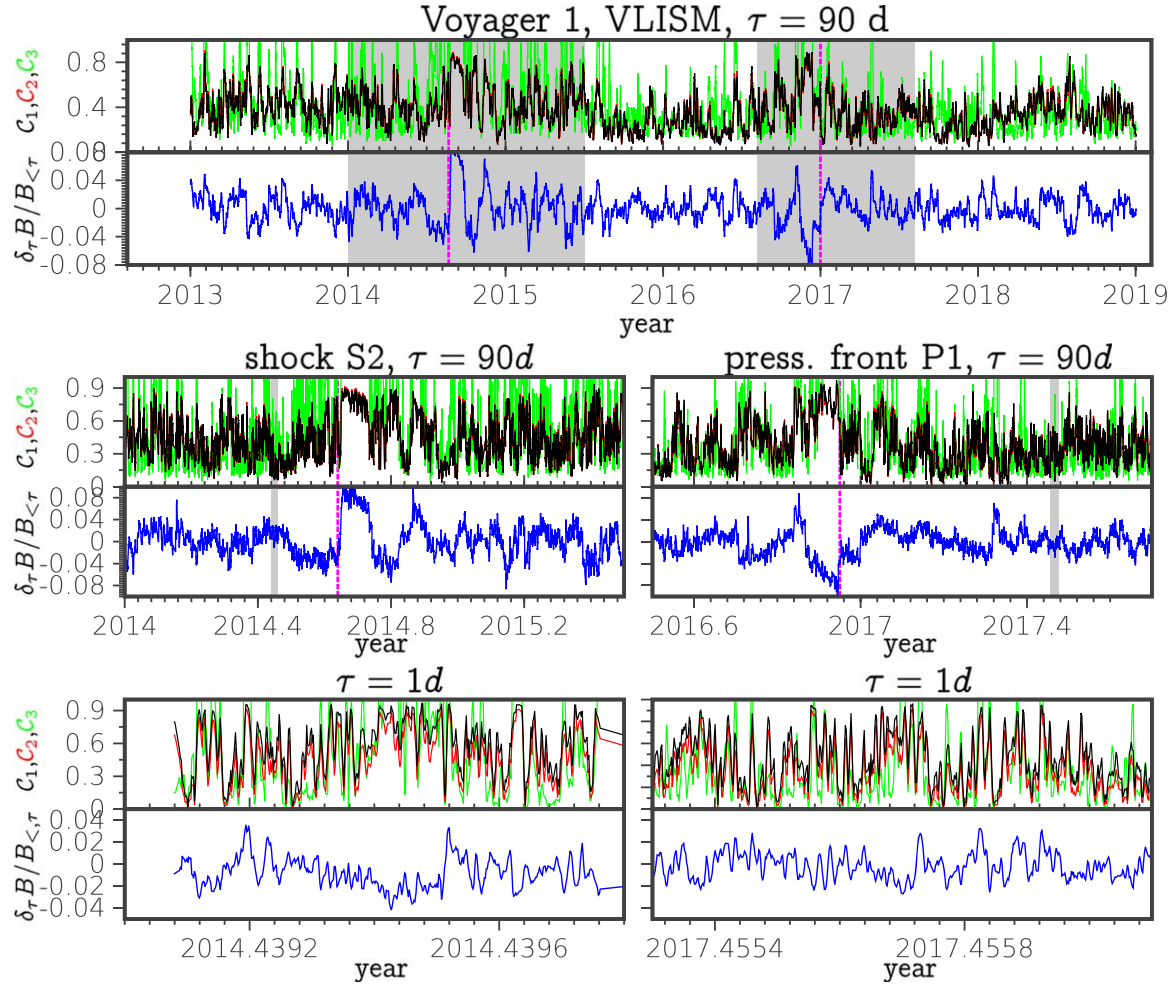


Figure 4. Magnetic compressibility as a function of time along the VI trajectory. The upper parts of each panel show magnetic compressibility calculated using different indicators, i.e., C_1 , C_2 , and C_3 (see Equations (3)–(5)). The lower parts of each panel show fluctuations of the magnetic field strength, normalized to the local average. Top panel: observations in the VLISM made during the years of 2013–2019. The filter width is chosen to be $\tau = 90$ days to highlight the large-scale anisotropy. All quantities are smoothed over 3 days for visualization purposes. The shaded regions, which contain S2 and P1, are magnified in the middle panels. Bottom panels: ~ 9 hr subsets are shown, magnification of the shaded bands in the middle panels. In these panels, $\tau = 1$ day and the smoothing window of 144 s is applied.

flow directions may be nearly orthogonal to the magnetic field, so that $(U_0-V_{\text{SC}})_{\parallel}\ll (U_0-V_{\text{SC}})_{\perp}$. This suggests that $\omega_{\text{SC}}\approx (\pm C_{wave}+V_{\text{rel}})\cdot k\approx (\pm C_{wave,\perp}-|U_R|-V_{\text{SC}})k_{\perp}=\widetilde{V}k_{\perp}$. The speed of fast-magnetosonic waves propagating outwards, as observed by VI, is then $\widetilde{V}\approx 16$ –22 km s⁻¹, whereas nonpropagating modes for which $C_{wave}=0$ in the plasma frame, have $\widetilde{V}\approx 24$ –30 km s⁻¹. Note that the difference between these two estimates is not large. Since $(|U_R|+V_{\text{SC}})$, C_A , C_f are close to each other (see Table 1), we do not expect the observed frequency spectra to be considerably distorted with respect to the real wavenumber spectra. Therefore, we provide a rough estimate of wavenumbers in the spectra shown in Figures 5–7 using the approximation $k_{\perp}\approx 2\pi f_{\text{SC}}/(|U_R|+V_{\text{SC}})$. Accordingly, also the length scale ℓ in the horizontal axis at the top of Figures 9 and 10 represents the perpendicular scale.

Moreover, since we consider broadband spectra and it is unrealistic to assume that $B(r) = B(t - r/\tilde{V})$, the question arises whether Taylor's approximation can at least be recovered in a statistical sense, i.e., whether $E(\omega_{SC}) \sim E(k)\delta(\omega_{SC} - k_{\perp}\tilde{V})$ for an appropriate speed \tilde{V} . We verified this fact by modeling a

synthetic turbulent 1D field in the quasi-linear statement similar to that in Klein et al. (2012).

The synthetic field is specified as

$$Q(x,t) = \sum_{m}^{M} \sum_{n}^{N} \hat{Q}_{mn} \exp[i(k_n x - \omega_{mn})t)], \qquad (7)$$

which is a linear superposition of M=2 different fields, each possessing a power-law spectrum with $N=2^{17}$ wavenumber components and a uniform-random distribution of the Fourier phases. The dispersion relation is specified as $\omega_m(k)=\pm [k^3E(k)]^{1/2}\pm V_{\rm rms}k+(U-V_{\rm SC})k+C_{{\rm wave},m}k$, which imitates the bulk flow, the sweeping effect by $V_{\rm rms}$, and both the nonlinear and linear components of the dispersion relation described above. The \pm sign indicates that both directions of propagation are included. Although performed in the anisotropy assumption, this analysis suggests that the observed frequency spectrum preserves the power law of the original wavenumber spectrum, thus excluding the possibility that the spectral broadening discussed later is due to the violation of Taylor's hypothesis.

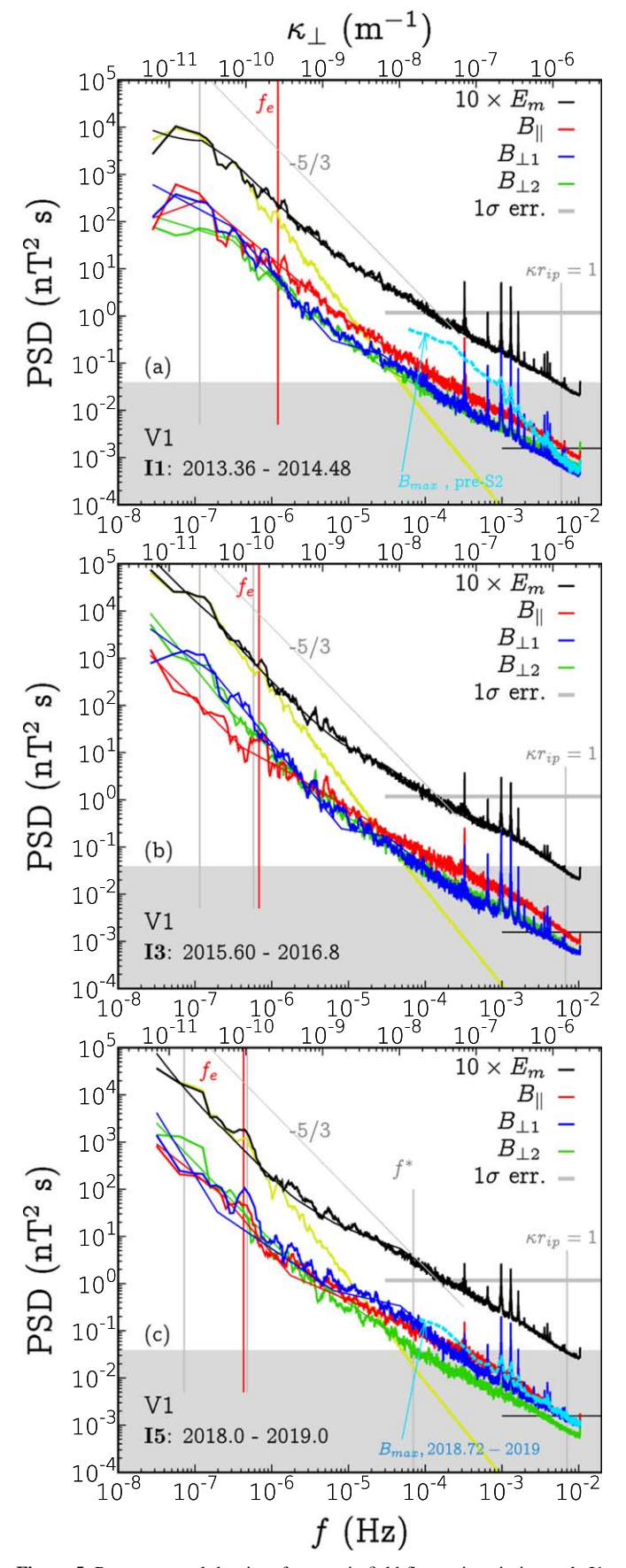


Figure 5. Power spectral density of magnetic field fluctuations in intervals I1, I3, and I5 (from the top to the bottom).

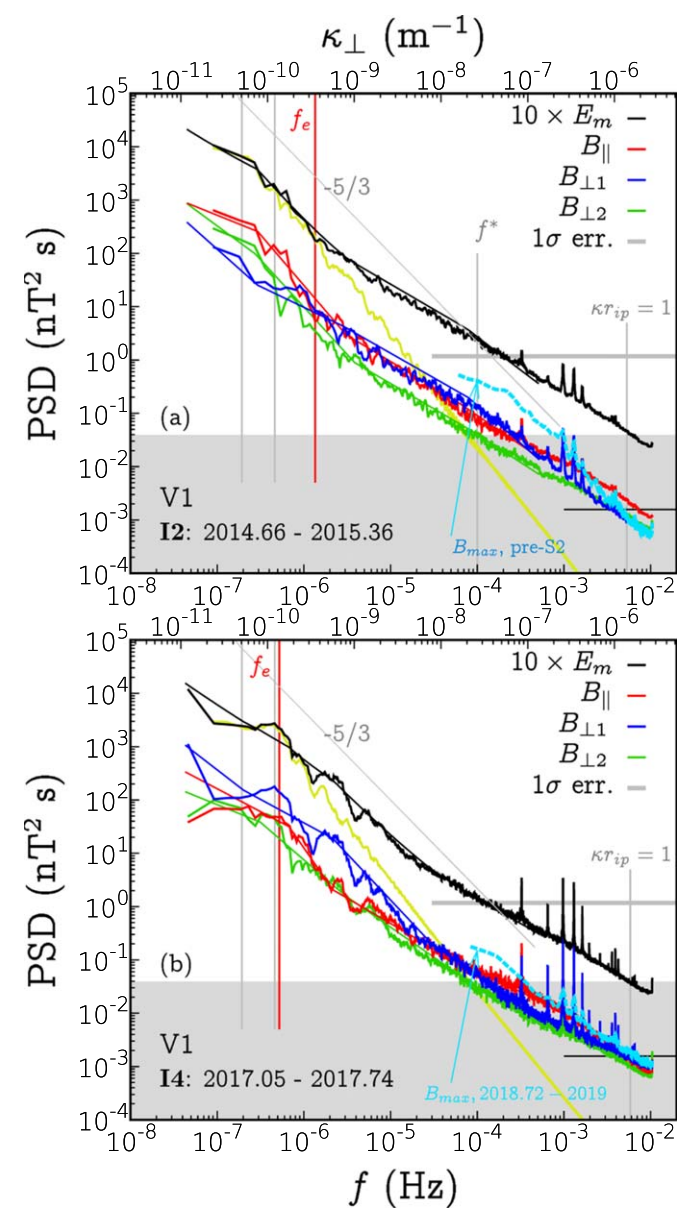


Figure 6. Power spectra in intervals I2 (top panel) and I4 (bottom panel).

4.2. Power Spectral Density of Magnetic Turbulence in the VLISM: The Low-frequency Range

Figure 5 shows magnetic energy power spectra for periods I1, I3, and I5, while Figure 6 shows the PSD for intervals I2 and I4, which involve compressed plasma behind shock/compression waves. The thick curves show the log-smoothed spectra from the *compressed sensing* technique (Donoho 2006).

The thinner smooth curves show the results of an iterative procedure based on synthetic turbulence sets. They provide us with a piecewise-linear spectrum that estimates how the PSD would behave in the absence of data gaps. A description of these spectral estimation methods can be found in Appendix A of Fraternale et al. (2019a) (see also Gallana et al. 2016; Fraternale et al. 2019b).

The accuracy of this technique in the high-frequency range was verified by comparing it with the well-known method of averaging the spectra of continuous subsamples. The application of different independent techniques is crucial for assessing

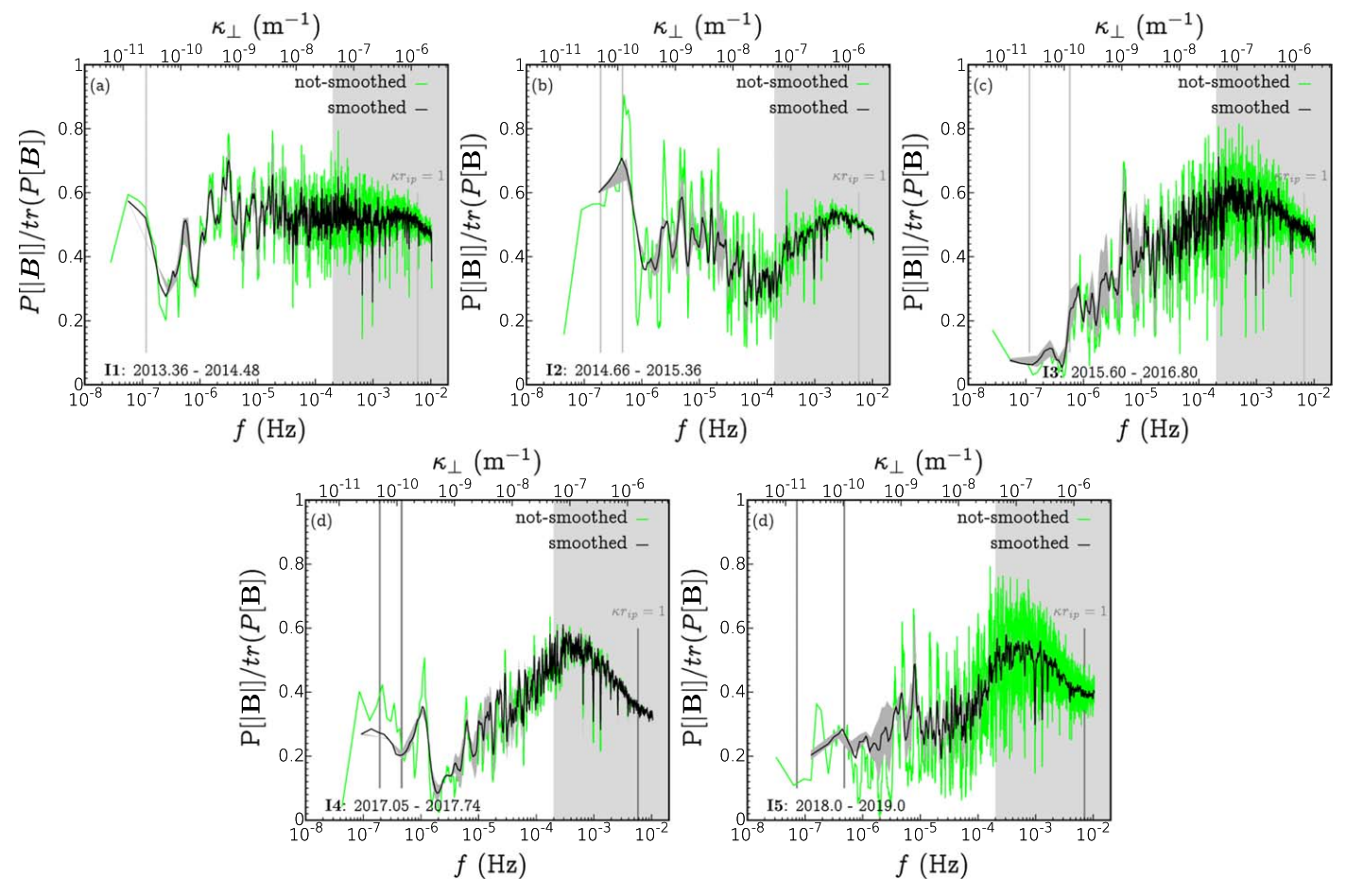


Figure 7. Magnetic compressibility in the Fourier space. Panels (a)–(d) show the results for intervals I1–I5. The vertical lines indicate large-scale periodicities shown also in Figures 5 and 6. The gray bands show the range of frequencies that are more likely to be affected by the nominal level of noise, as shown Figures 5 and 6.

uncertainties related to missing data in the Voyager time series. In this regard, the intermediate range of frequencies, $f \in [10^{-5}, 10^{-4}]$ Hz, is the most critical for recovery. Hereinafter, f is the frequency in the spacecraft frame. All spectra display sharp spikes at frequencies $f = j \cdot 3.26 \times 10^{-4}$ Hz (j = 1, 2, 3, ...), which are due to the instrumental effects. These frequencies remain unchanged inside all intervals considered in this paper. These instrumental spikes are also present in the IHS data, as shown in Fraternale et al. (2019a, 2019b).

The gray bands in all panels of Figures 5–7 and 9 show the 1σ uncertainty, which is modeled as white noise with amplitude $A=0.035\,\mathrm{nT}$, so that $P_{\mathrm{noise}}=2\Delta t_sA^2/3=0.04\,\mathrm{nT}^2\,\mathrm{Hz}^{-1}$. The nominal magnetometer noise level ($A=0.005\,\mathrm{nT}$) is also shown with the black horizontal line. Note that we used $\Delta t_s=48\,\mathrm{s}$ for the estimate of P_{noise} , which is a conservative estimate since the actual sampling time is smaller. It is expected that the fluxgate magnetometers have a 1/f noise component, as suggested by the flattening of all spectra in the high-frequency regime.

The power spectrum in the low-frequency regime $(f \lesssim 10^{-6} \, \mathrm{Hz})$ is found to follow a power-law decay $P \sim f^{-\alpha}$ with spectral index α , which reaches values as high as 2. In this regime, turbulence coexists with large-scale wave structures shown in Section 3, which dominate the spectrum. Quasiperiodic correlation scales shown in Figure 3 can be also distinguished in the unsmoothed spectrum (not shown here). They are indicated in Figures 5 and 6 with vertical gray lines in the low-frequency range.

We can evaluate the causality condition (the age of fluctuations) for fluctuations transmitted from the IHS into the VLISM and traveling outwards. To participate in an active turbulent cascade, the waves detected by the spacecraft should have evolved for at least one nonlinear timescale since their origin at the HP. Let us consider the nonlinear time, "eddy turnover" time $\tau_{nl}\approx 2\pi r/\delta v$, and propagation speed $(C_{\rm f}-|U_R|)$ in the fixed frame. Then, the threshold size corresponding to one eddy turnover, r_e , and the corresponding frequency in the VI frame, f_e , can be obtained as

$$r_e = \frac{\delta v (d_{\rm SC} - d_{\rm HP})}{2\pi (C_f - |U_R|)},\tag{8}$$

$$f_e = \frac{|C_f - |U_R| - V_{SC}|}{r_e}.$$
 (9)

The choice of $\delta v \approx \delta b = 3 \, \mathrm{km \ s^{-1}}$ yields the cutoff frequency $f_e \approx 10^{-6}$ Hz, which decreases with the heliocentric distance, as shown in Figures 5 and 6 with vertical red lines.

Fluctuations of the longitudinal component are dominant in interval I1, as can be seen from Figure 5(a) (Burlaga et al. 2015). The spectral index of B_{\parallel} is $\alpha_{\parallel}=1.4\pm0.15$, in the frequency range $f\in[8\times10^{-8},\ 10^{-6}]$ Hz (the reported uncertainties include both the effect of the log-log fit and discrepancy between the techniques). After the initial flatter range, the transverse components steepen to $\alpha_{\perp}=1.8\pm0.15$ until further flattening occurs around 5×10^{-6} Hz.

A relatively fast decay of the incompressible components is also found in interval I3, where $\alpha_{\perp 1}=2.05\pm0.20$ and $\alpha_{\perp 2}=1.93\pm0.15$ for frequencies $f\in[8\times10^{-8},\,10^{-6}]$ Hz. In the same frequency range, $P[B_{\parallel}]$ is shallower with $\alpha_{\parallel}=1.35\pm0.15$ and its values are similar to those in intervals I1 and I5. Note, however, that $P[B_{\parallel}]$ is smaller by a factor of $\sim\!8$ as compared with the transverse components. The increase in energy density observed in the large-scale, transverse fluctuations and the relatively large spectral index are related to the structures shown in Figure 2(a).

In I5, the spectrum of B_{\parallel} exhibits the spectral index higher than that in I3, with $\alpha_{\parallel}=1.85\pm0.15$ in the range of $f\in[8\times10^{-8},\ 10^{-6}]$ Hz. This is due to a few relatively intense magnetic pressure pulses present in this interval, as shown in the top panel of Figure 4. An abrupt flattening is then observed for $f\gtrsim10^{-6}$ Hz. The transverse components show a similar scaling. A broad bump is observed in the spectrum of B_{\parallel} and $B_{\perp 1}$. It is centered at $f\approx5\times10^{-7}$ Hz ($\tau\approx16$ –34 days). This is related to the mixture of transverse and longitudinal fluctuations seen at the beginning of 2018, and compression waves present in 2018 (see Figures 2(c) and 4, top panel).

To highlight the contribution of large gradients and N-shaped profiles in the magnetic field distribution, we computed the PSD of a "ramp-jump" signal which approximates the large-scale field, similarly to what was done earlier by Roberts & Goldstein (1987) for the SW. Here, the points of the most significant/abrupt change in the signal are identified for each component of \boldsymbol{B} by the automatic procedure described by Killick et al. (2012). In this procedure, a piecewise-linear signal, which approximates the large-scale distribution of \boldsymbol{B} , is obtained and its power spectrum is computed. The trace of this spectrum is shown with yellow curves in Figures 5 and 6. It has a spectral index close to \sim 2. By comparing this spectrum with the total magnetic energy spectrum (black curves), we arrive at the conclusion that the contribution of random fluctuations becomes dominant for frequencies larger than \sim 10⁻⁶ Hz.

Inspecting the magnetic field power spectra in periods I2 and I4, shown in Figure 6, one can see flat spectra at $f \lesssim 5 \times 10^{-7}$ Hz for both time intervals. They are followed by steep cascades of the longitudinal component with $\alpha_{\parallel}=2\pm0.15$ in the range of $f \in [5 \times 10^{-7}, 2 \times 10^{-6}]$ Hz. The bumps in the spectrum reflect the presence of waveforms shown in Figures 2(b) and (d) 4. While $B_{\perp 2}$ exhibits similar scaling, $B_{\perp 1}$ behaves differently in both intervals. In I2, once the low-frequency peaks are gone, this component maintains a relatively high level of power and dominates the intermediate range of frequencies $10^{-6} \lesssim f \lesssim$ 10^{-4} Hz. In I2, the maximum variance direction is $\hat{e}_{\text{max}} = (-0.005, 0.918, 0.397)$ (in the *RTN* frame), which is consistent with the observed large-scale fluctuations of |B|. If the signal is processed with a high-pass filter and only small scales with $f > 5 \times 10^{-5}$ Hz are retained, we obtain $\hat{e}_{\text{max}} = (0.064,$ -0.68, 0.73). Note also that $\hat{e}_{\parallel} = (-0.318, 0.866, -0.385)$ and $\hat{e}_{\perp 1} = (-0.133, 0.361, 0.922).$

The situation is different in I4, where $B_{\perp 1}$ dominates for both large and intermediate scales. The spectral index in the range $f \in [2 \times 10^{-6}, 2 \times 10^{-4}]$ is $\alpha_{\perp 1} = 1.62 \pm 0.05$, and a flatter regime is found at lower frequencies. Broad spectral bumps are observed at $f \approx 2 \times 10^{-6}$ Hz for $B_{\perp 1}$ only, whereas it occurs at $f \approx 5.5 \times 10^{-7}$ Hz for all other components. As before, this is related to the presence of wave structures found in the post-P1 region (partially shown in Figure 2(b)).

4.3. PSD of Magnetic Turbulence in the VLISM: Intermediateand High-frequency Ranges

One can see that all spectra flatten at frequencies exceeding $\sim 10^{-6}$ Hz, where the spectral index becomes near 1. Although the smallness of spectral index is likely due to data uncertainties in the high-frequency interval $f \gtrsim 10^{-4}$ Hz, it is not clear if the 1/f extends down to frequencies as low as 10^{-6} Hz. It is significant, however, that variance anisotropy is observed in the intermediate- and high-frequency ranges.

When considering the 2014.65 shock, Fraternale et al. (2020) determined that transverse, small-scale fluctuations of B are as intense as 10% of the mean field. They start abruptly on DOY 177, 2014 and gradually decrease in intensity until 2015. The initial enhancement is possibly induced by kinetic processes occurring in the foreshock region, where the fluctuations seem to be compatible with a filamentary topology. An example of such behavior is shown in panel (g) of Figure 2. Remarkably, a spectral break exists at $f^* \approx 1.5 \times 10^{-4}$ Hz ($\ell_{\perp} \approx 10^{-3}$ au), where the spectrum changes from a $\sim 1/f$ regime to a Kolmogorov-like power law. The intensity of this event allows us to see the intermittent nature of the field in the small-scale regime. This explains the variance anisotropy in interval I2 (Figure 6(a)), which includes the aftershock region. The spectrum of the maximum variance component in the foreshock region of S2 (2014.486-2014.61) is shown with the cyan dashed curves in Figures 5(a) and 6(a) for comparison. It is clear that the turbulent cascade in this interval has dissipation rate differing from that observed on the large and intermediate scales, which is also seen in Figures 9(a) and (b). In other words, local processes (in the wavenumber space) seem to be active on these scales and determine the large separation between macro- and microscales of the spectrum.

As discussed in Section 3, similar small-scale structures are observed in late 2018 (see Figure 2(i)). Moreover, the level of turbulence makes it possible to detect small-scale intermittency during this period. From Figure 8, one can see that the kurtosis of magnetic field increments reaches the value of 5 for transverse fluctuations. Unlike the 2014 shock event, the enhancement of turbulence in 2018 does not occur abruptly on a specific day. Moreover, it does not seem to be directly related to a particular shock wave. However, one cannot exclude that some magnetic field lines are connected to a shock surface far from VI.

In the 2018.72–2019.0 interval, the maximum variance direction of fluctuations with $f > 10^{-4}$ Hz is $\hat{e}_{\text{max}} = (0.007, -0.39, 0.92)$. The fluctuations have both transverse and compressible nature, and a correlation of 0.25 is found between δB_{\parallel} and $\delta B_{\perp 1}$. The spectrum of B_{max} ($\sim B_{\perp 1}$) for the time interval 2018.72–2019.0 is shown with the dashed cyan curve in Figures 5(c) and 6(b). One can see that the spectral index is ~ 1.7 in the narrow frequency range of $f \in [2 \times 10^{-4}, 8 \times 10^{-4}]$. For this reason, it is possible that a mild spectral break of $B_{\perp 1}$ observed in I5 at f^* is physically significant and can be related to rapid variations of this component. In any event, it should be expected that the actual turbulent spectrum in this regime is steeper than in the observations, which are likely affected by the data noise.

A smooth change in the power law in the high-frequency range is also observed in the spectrum of longitudinal fluctuations, at frequencies larger than f^* . For instance, steepening of $P[B_{\parallel}]$ is observed in intervals I3 and I4 at $f \gtrsim 10^{-3}$ Hz. It is of interest that the perpendicular components in I3 are weaker by a factor of \sim 5 in the high-frequency regime

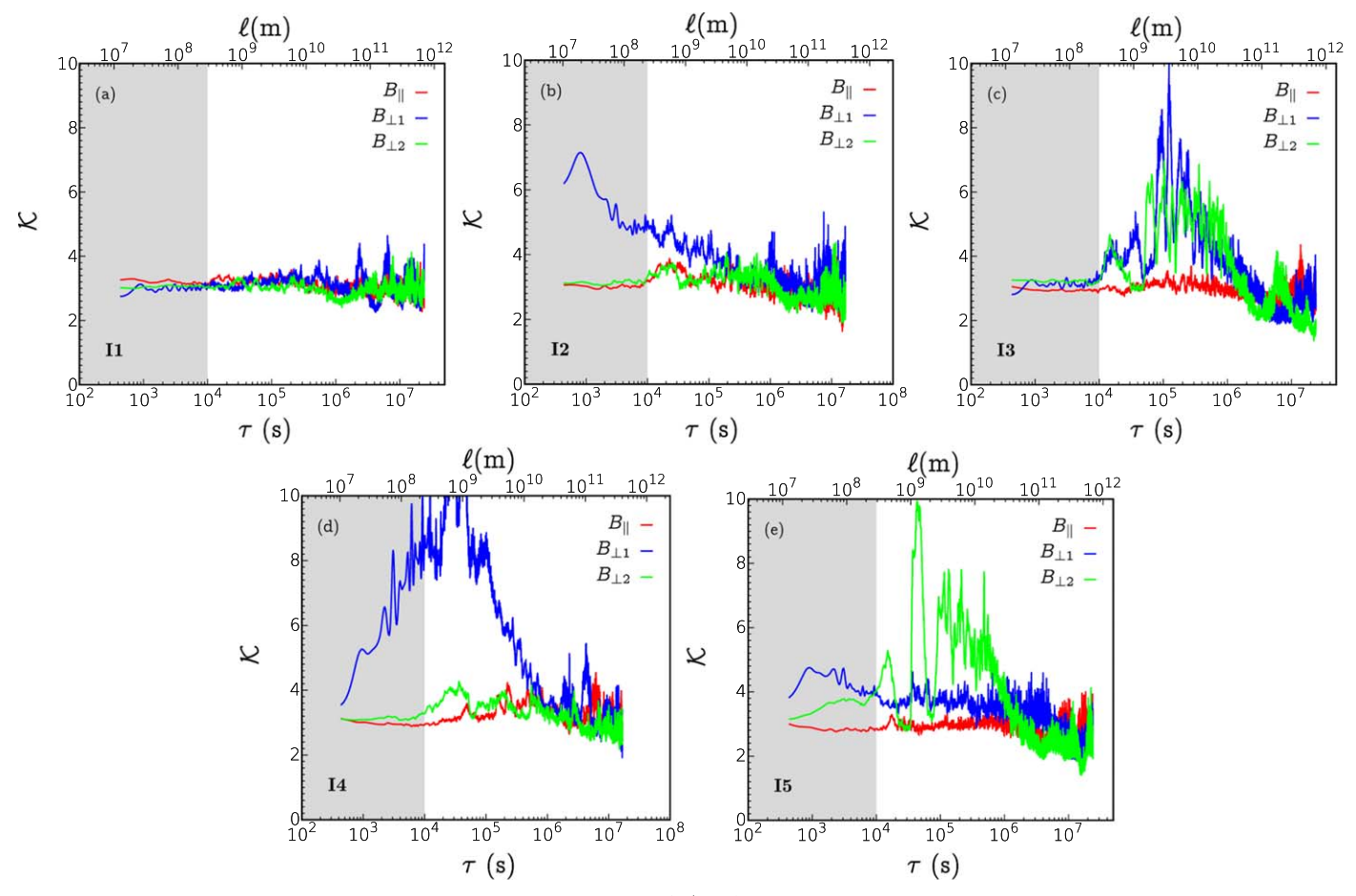


Figure 8. Scale-dependent kurtosis of magnetic field increments, $\mathcal{K}[B_j] = \langle \Delta B_j^4 \rangle / \langle \Delta B_j^2 \rangle^2$, obtained from 288 s averaged data. Panels (a)–(d) show the results for intervals I1–I5.

as compared with the longitudinal component. In fact, the variance anisotropy is such that the longitudinal component dominates during the last spectral decade in all intervals. This is illustrated in Figure 7, which shows the scale-dependent magnetic compressibility, C(f). The increase in C with increasing frequency is observed in all chosen time intervals except I1, where the compressibility is large for the whole spectrum. It is unlikely that such trend is due to noise in the data. It is worth noting that growing compressibility was also observed in the inertial range of IHS turbulence (Fraternale et al. 2019a, 2019b). Its reduction with distance is observed in the large and intermediate frequency ranges, where C drops to values of around 0.2. The maximum value of \sim 0.6 is reached in the high-frequency range at about 5×10^{-4} Hz. It is likely that the subsequent decrease is an artifact of data noise, although the anisotropy is clearly still strong in this regime. At large scales, higher magnetic compressibility observed in I1 is consistent with the previous observations (Burlaga et al. 2015). Relatively low compressibility in later intervals I3 and I5 was also observed by Burlaga et al. (2018, 2020a) and Zhao et al. (2017). Using a three-wave interaction model, Zank et al. (2019) demonstrated that the fast-magnetosonic modes transmitted across the HP may decay into Alfvénic fluctuations within 1–10 au from the HP for $k \in [10^{-11}, 10^{-10}]$ m⁻¹. Here we extend the observational range to frequencies higher than 10^{-5} Hz and show that (i) relatively large values of \mathcal{C} persist in the high-frequency regime in all intervals; (ii) due to the

presence of large-scale compressible fluctuations in 2018–2019 (as shown in Figure 7), \mathcal{C} is higher in I5 than in I3 on large scales; and (iii) the decrease in \mathcal{C} seems to be related to the increase of transverse fluctuations, rather than to the decay of parallel fluctuations (see also Figure 10).

4.4. Intermittency and Third-order Moments

Magnetic turbulence intermittency (see Kolmogorov 1962; Obukhov 1962; Frisch 1995, and Sorriso-Valvo et al. 1999 for the SW context) is investigated by analyzing the scale-dependent kurtosis of magnetic field temporal increments with the time lag τ , $\Delta_{\tau} \mathbf{B} = \mathbf{B}(t) - \mathbf{B}(t+\tau)$, as seen in Figure 8. Our analysis complements the recent study by Burlaga et al. (2020b) dedicated to intermittency of hourly increments. The computation of highorder statistics is challenging. We investigated the convergence and accuracy of the empirical moments with the methods described by Dudok de Wit (2004) and Podesta et al. (2009), and discuss it in Appendix B, see Figures 11 and 12. It is clear that the longitudinal component is typically non-intermittent with kurtosis $\mathcal{K}[B_{\parallel}](\tau) = \langle \Delta_{\tau} B_{\parallel}^4 \rangle / \langle \Delta_{\tau} B_{\parallel}^2 \rangle^2 \approx 3$. In the intermediate range of scales, instances of intermittency with kurtosis values up to 10 are observed for transverse fluctuations, especially in intervals I3, I4, and I5. Data gaps may contribute to the enhancement of oscillations of K in this range, but the gaps themselves do not generate intermittency. Clearly, coherent

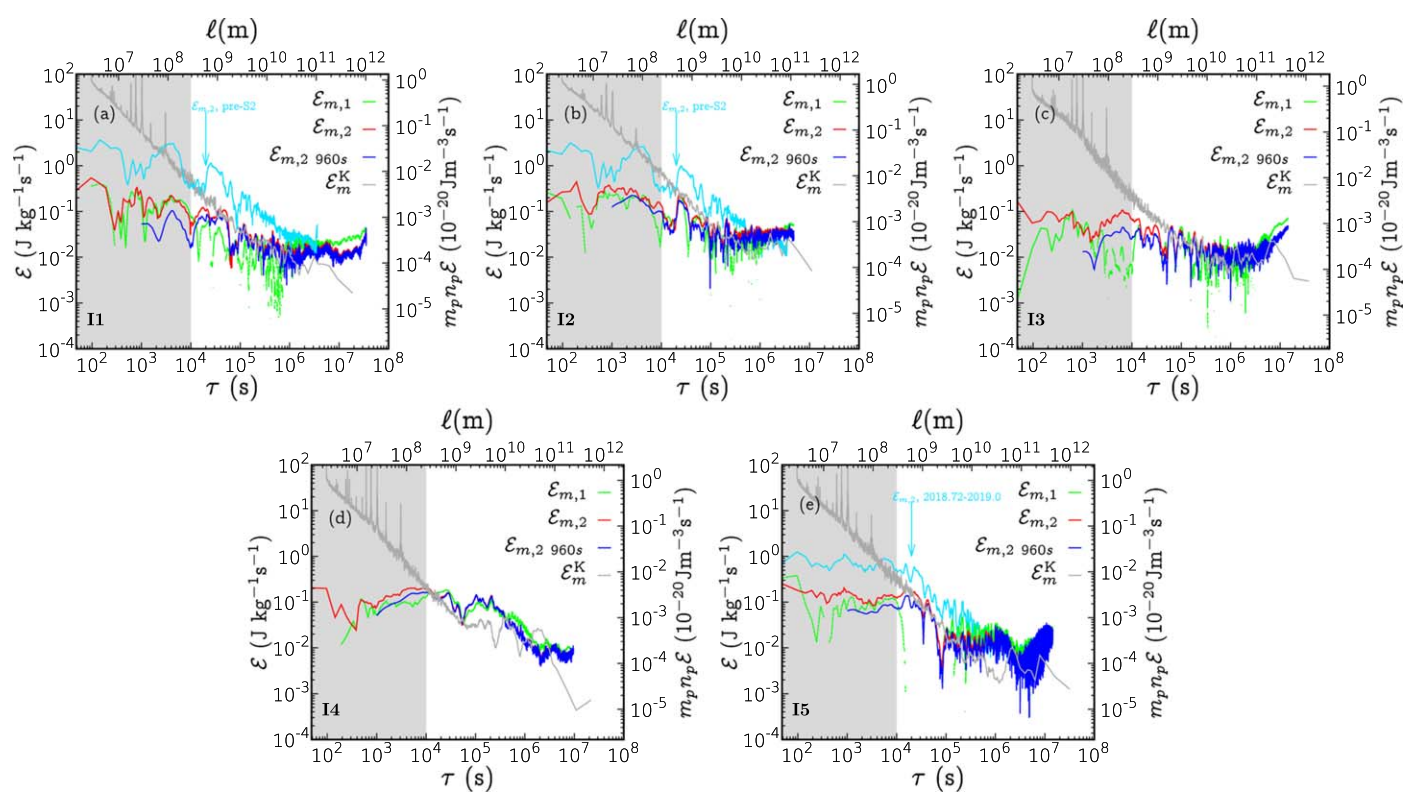


Figure 9. Third-order moments, computed using Equations (11) (green curves) and (12) (red curves for 48 s data and blue curves for 960 s averaged data). Panels (a)–(d) show the results for intervals I1–I5. For comparison, the gray curves show the result based on Equation (13). The light blue curves show the third-order moment in the pre-shock interval in front of S2 (panel (a)), and in the second-half of 2018 (panel (e)), where enhanced fluctuations have been observed (see the light blue spectra of Figures 5 and 6(a) and (c)).

structures and steep profiles contribute significantly to such intermittency (see Figure 2).

The absence of intermittency during I1 may be related to younger turbulence generated by the forcing effect of the HP fluctuations (e.g., Zank et al. 2017). These fluctuations are likely to be superimposed with the pristine interstellar turbulence and interact with it. In the immediate vicinity of the HP, the pristine turbulence is not resolved, remaining below the instrumental threshold. Nevertheless, a few peaks in kurtosis are present around the value of \sim 4 for large scales. These are due to the presence of steepened waves. As discussed in Section 3, intermittent transverse fluctuations are found in the small-scale regime during 2014.5-2015 and in late 2018. This can be seen in panels (b) and (e) of Figure 8. These are the only periods where the kurtosis grows in the noisy band. The intermittency of δB_{\parallel} is hardly observed anywhere. As was earlier discussed by Fraternale et al. (2020), one cannot exclude that small-scale intermittency is hidden within data noise. The role of intermittency in the interstellar turbulence remains the subject of additional future investigations. Time-dependent effects are of substantial importance in the VLISM. Moreover, the observed turbulence is still far from being homogeneous.

We analyze the scale-dependent, *signed*, third-order moments of magnetic field fluctuations, shown in Figure 9. In particular, we compute the vector moments,

$$\mathcal{F}_{m}(\tau) = \langle \|\boldsymbol{\Delta}_{\tau}\boldsymbol{b}\|^{2} \Delta_{\tau}\boldsymbol{b} \rangle. \tag{10}$$

Here $\mathbf{b} = \mathbf{B}/(\mu_0 \rho_0)^{1/2}$ is magnetic field expressed in the Alfvén units, $\Delta_{\tau} \mathbf{b} = \mathbf{b}(t) - \mathbf{b}(t+\tau)$ is the temporal increment for a time lag τ , representing, under the Taylor's approximation, a spatial increment in the direction of relative motion

(approximately in the radial direction). The corresponding spatial scale is then $\ell \approx \tau V_{\rm rel}$.

From the moments of Equation (10) we obtain the following estimates for the magnetic energy per unit time and mass:

$$\mathcal{E}_{m,1}(\ell) = 3/4 \langle \| \boldsymbol{\Delta}_{\tau} \boldsymbol{b} \|^2 \Delta_{\tau} b_{\ell} \rangle / \ell, \tag{11}$$

$$\mathcal{E}_{m,2}(\ell) = 1/4 \sum_{j=1}^{3} |\langle \| \boldsymbol{\Delta}_{\tau} \boldsymbol{b} \|^{2} \Delta_{\tau} b_{j} \rangle | /\ell, \qquad (12)$$

where $\Delta_{\tau}b_{\ell}$ is the component of magnetic field increment in the direction of relative motion. The first quantity (green curves in Figure 9) resembles the Monin–Yaglom 4/3-law derived from the Kármán–Howarth equation describing the average energy dissipation rate per unit mass in hydrodynamic homogeneous turbulence (see, e.g., Equation (22.15) in Monin & Yaglom 1971). The second quantity is simply the average of all three components of \mathcal{F} . It is shown with red and blue curves in Figure 9. The MHD analog of the 4/3-law was first derived by Politano & Pouquet (1998) (PP), and is now widely used in the studies of the SW turbulence (e.g. Sorriso-Valvo et al. 2007; MacBride et al. 2008, and the review by Coburn et al. 2015), and more recently of the magnetospheric turbulence (e.g., Hadid et al. 2018; Sorriso-Valvo et al. 2019; Bandyo-padhyay et al. 2020)

The PP law involves mixed velocity and magnetic moments. Therefore, it is clear that Equations (11) and (12) do not represent the dissipation rate of turbulent energy, regardless of having the energy dimension. However, these terms may still provide better order-of-magnitude estimates for the magnetic energy flux than other proxies relying on the second-order

moments (see Equation (13)). Note that this is the first attempt to compute third-order statistics using Voyager data in the VLISM. It may be also of interest that $\mathcal{F}_{m,1}$ appears in the expression describing the cascade rate of cross helicity, as shown by Podesta (2008). Magnetic moments also appear in the Hall-MHD extension of the PP law (Galtier 2008). However, our primary intention here is to highlight the scaling properties of magnetic field turbulence.

Let us compare expressions (11) and (12) with the proxy based on the unidirectional magnetic spectrum (gray curves in Figure 9), which is given by

$$\mathcal{E}_{m}^{K}(f) = A \left(\frac{2\pi}{V_{\text{rel}}}\right) f^{5/2} \left(\frac{E_{m}(f)}{\mu_{0} m_{p} n_{p}}\right)^{3/2},$$

$$A = [5/3(1 + R_{A})/C_{K}]^{3/2},$$
(13)

where R_A is the Alfvén ratio and $C_K = 1.6$ is the Kolmogorov constant (we set $R_A = 0.5$, but the actual value is unknown). In addition, $E_m = 1/2\sum_j^3 P[B_j]$ is (half) the trace of the magnetic spectral matrix. Equation (13) is based on the dimensional analysis and assumption of the Kolmogorov spectrum in the inertial subrange. The analogous expression in hydrodynamic turbulence traces back to Kovasznay (1948). Despite roughness of the estimate provided by Equation (13), it has been widely used to estimate the dissipation rate of turbulence in the SW (e.g., Leamon et al. 1999; Smith et al. 2006; Cannon et al. 2014) and in the VLISM (Florinski et al. 2016).

We compute \mathcal{F} from 48 s VI data without either interpolation or reconstruction of the missing data. The signed statistics should reduce to some extent the effect of uncorrelated noise in the small-scale range. We compare $\mathcal{E}_{m,2}$ computed from 48 s data (red curves) and from 960 s averages (blue curves), the latter reducing the effect of noise. The two moments show differences in the gray band only, as expected. However, $\mathcal{E}_{m,960s}$ is smaller than $\mathcal{E}_{m,48s}$ by a factor \sim 2 in the time intervals with larger discrepancy.

Our analysis shows that the third-order magnetic moments are nearly constant in both the intermediate- and small-frequency ranges, as expected for the inertial range of turbulence. Note, however, that the values are different in these two regimes, the high-frequency range displaying the level higher by a factor of $\sim \! 10$. This is consistent with the shape of observed power spectra.

In the intermediate range of scales $(10^5 \lesssim \tau \lesssim 10^7 \text{ s})$, the spectral proxy from Equation (13) provides us with a similar estimate. The values of $\mathcal E$ in this range are about $(1-5) \times 10^{-2} \, \text{J kg}^{-1} \text{s}^{-1}$ for the rarefied periods and slightly higher in the compressed periods. The corresponding rate per unit volume in cgs units is about $(1.5-8) \times 10^{-23} \, \text{erg cm}^{-3} \text{s}^{-1}$.

At smaller scales, we observe the flux increase to values near 0.1 J kg⁻¹s⁻¹ (\sim 1.7 \times 10⁻²² erg cm⁻³s⁻¹). Interestingly, at small scales and for $48 \lesssim \tau \lesssim 10^4$ s, the fluxes computed with the signed moment remain nearly constant, while \mathcal{E}_m^R grows to much larger values as a consequence of the shallower power spectrum in this regime. A similar trend is shown in the absolute third-order moments of magnetic fluctuations. The cyan curves in panels (a) and (b) report the cascade rate computed in the pre-shock region of S2, displaying a 10-fold enhancement with respect to the earlier period I1. The cyan curve in panel (e) shows the increased rate, which is also seen in late 2018. In these cases, $\mathcal{E}_m \approx 1$ J kg⁻¹ s⁻¹.

5. Discussion and Summary

We have analyzed magnetic field fluctuations in the VLISM over a broad range of spacecraft-frame frequencies ranging from 2×10^{-8} Hz to 0.02 Hz, which correspond to spatial scales from \sim 7 au to \sim 1500 km and extended upon our previous analysis in Fraternale et al. (2019a). We subdivide the 6 yr period of V1 observations (2013.36–2019.0) into three intervals of less intense magnetic field and two intervals of stronger field, i.e., the regions downstream of the 2014.65 shock and the 2017.0 pressure front. We have shown that the ISMF in the VLISM exhibits quasiperiodic, wave-like structures with periodicity ranging from 15-100 days. These are clearly seen from the analysis of two-point correlations. A low-frequency break in the statistics is observed in all chosen time intervals, including the "quiet" intervals considered by Burlaga et al. (2018). This speaks in favor of the scenario where the heliospheric forcing dominates the spectrum of VLISM turbulence on the scales considered in this paper (see also Matsukiyo et al. 2019; Zank et al. 2019). This can also be seen in the normalized structure functions presented in Figure 10.

We have shown that large-scale magnetic field profiles are inhomogeneous and frequently display an N-like shape and mixed longitudinal/transverse nature, which is indicative of nonlinear wave steepening (Whitham 1974). This feature was earlier predicted in the numerical simulations of Kim et al. (2017), which show compressible perturbations overtaking each other. Although the accuracy of V1 MAG observations (Burlaga & Ness 2016; Burlaga et al. 2019), intrinsically representing a linear time series, is inconclusive in this respect, it is hard to imagine that shock-on-shock overtaking and interaction do not occur in the VLISM. The two-step magnetic field profile making pressure front P1 is a likely manifestation of such a process. Interestingly, the spectral density of the field strength, which serves as a proxy for compressible fluctuation modes, is higher in 2018 than in 2016, and is comparable to the values observed in 2013. The increased power of transverse fluctuations detected in 2015 by Burlaga et al. (2018) is largely related to a quasiperiodic structure with a \sim 100 day period. Although the data uncertainty for B_R is large, the profiles of B_R clearly resemble nonlinearly evolved Alfvénic perturbations associated with weak directional discontinuities of thickness of \sim 10–20 r_{ip} . We found similar profiles in 2018. It should be noted that the intermittency of observed turbulence (Fraternale et al. 2019a) is associated with these structures and steep profiles.

The VLISM plasma has long been known to be collisional (e.g., Fahr & Ripken 1984). Recent V2 observations (Richardson et al. 2019), as well as earlier simulations of the SW-LISM interaction (Pogorelov et al. 2015, 2017b) state that the plasma temperature on the LISM side of the HP is $T \sim 30,000$ K. We have derived the mean-free paths and transport coefficients in the LISM plasma using the properties of Coulomb collisions (see Table 1). The mean-free path length of \sim 2–4 au is larger than the 0.25 au obtained in Mostafavi & Zank (2018) using T = 7,500 K. Both values exceed most of the scales observed in the spectrum of fluctuations. The collisional transport theory holds if the scale associated with gradients in the direction perpendicular to B is much larger than the geometric average between the mean-free path and the gyroradius $\sqrt{\lambda r_c}$, while the scale of parallel gradients exceeds λ . Since the spacecraft trajectory is nearly perpendicular to ISMF lines, in the

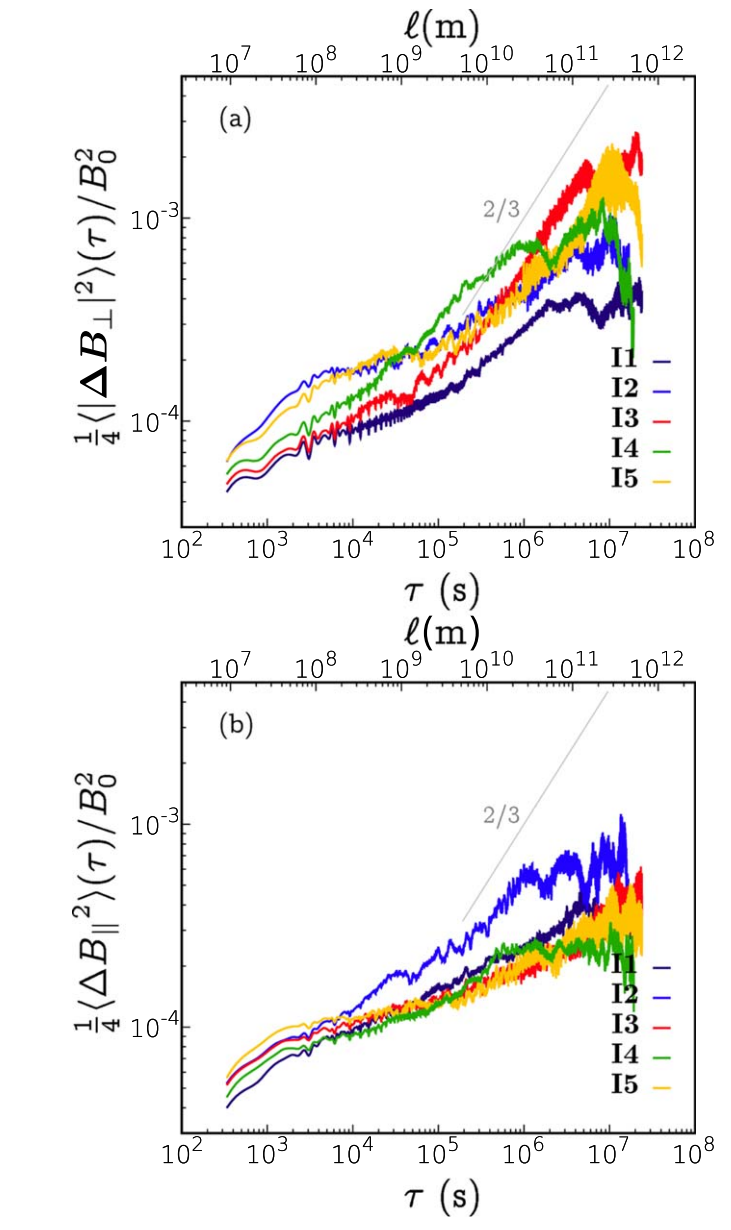


Figure 10. The second-order structure function for perpendicular (top panel) and parallel (bottom panel) fluctuation, normalized to the constant value $B_0 = 0.45$ nT. The quantity $\Delta \pmb{B} = \pmb{B}(t) - \pmb{B}(t+\tau)$ is the magnetic field vector increment as a function of the time lag τ . To reduce the data noise, 288 s averaged data was used, thus reducing the intensity of small-scale fluctuations by a factor of ~ 1.5 as compared with 48 s data. The factor of 1/4 is introduced to facilitate the comparison with Table 2 and literature analysis discussing the variance.

assumption of wavenumber anisotropy, we conclude that small-scale fluctuations with $\ell \gtrsim 100~r_{ip}$ satisfy the former condition. The latter condition cannot be verified at this point, and requires further analysis.

As shown in Table 2, the Reynolds number $Re = U_{\rm ref} L_{\rm ref}/D_{\mu}$ is rather small, being around 50–145 if estimated with the reference length and velocity equal to $L_{\rm ref} = 100$ au and $U_{\rm ref} = 25$ km s⁻¹, respectively, and the Braginskii parallel viscosity coefficient (the dominant term of the viscosity tensor, see Equation (A8)). Clearly, Re is higher (1500–2700) for $T \approx 7,500$ K. The magnetic Reynolds number $Re_m = U_{\rm ref}/D_{\eta}$ is much larger than Re, its values being in the range of 8×10^{13} – 5×10^{14} , in agreement with the estimates of Baranov

& Ruderman (2013). An effective magnetic Reynolds number related to large-scale fluctuations is $Re_{m,\rm eff} = (\ell_c/r_{ip})^{4/3} \sim 10^7$. It is constructed of the actual correlation scale of observed fluctuations and the ion inertial length, the latter being the scale where dissipative processes start to be significant. This expression has been used in SW studies since Matthaeus et al. (2005) (see also Weygand et al. 2007). It is analogous to that in hydrodynamics, where the dissipation scale is the Kolmogorov scale $\lambda_{\rm K}$ and $\lambda_{\rm K}/\ell = Re_\ell^{-3/4}$. Note also that the sonic Mach number based on the bulk flow, $M = U/C_s$, is estimated to be around 0.5, and the magnetic turbulent Mach number based on the rms of magnetic fluctuations, $M_{\rm turb} = \delta \ b_{\rm rms}/C_s$, is around 0.05 (Table 2).

It is clearly difficult to fit all V1 observations into the currently existing theoretical models. A Kolmogorov-like scaling $P(k_{\perp}) \sim k_{\perp}^{-5/3}$ of the perpendicular cascade is supported by the anisotropic and incompressible model of Goldreich & Sridhar (1995) (GS95), which assumes a "critical balance" between the dynamic and linear timescales, $(k_{\perp} \delta w)^{-1}$ and $(k_{\parallel}C_{\rm A})^{-1}$. For the correlation scales found in the presented analysis, GS95 implies that $k_{\perp}/k_{\parallel} \approx C_{\rm A}/\delta$ b_{rms} \approx 30. In the presence of compressible fluctuations, the situation is complicated by the difficulty to separate interacting compressible and incompressible modes. In principle, fast modes in collisionless plasmas should scatter more than the other modes, and consequently be more isotropic with respect to wavenumbers and have a shallower spectrum, provided that the wave propagation time $\sim (kC_f)^{-1}$ is chosen as a typical time of interaction between perturbations. This results in a $P(k) \sim k^{-3/2}$ spectrum, similarly to the acoustic turbulence in hydrodynamics. This may be a plausible explanation of the shallower spectrum of B_{\parallel} observed on large scales in interval I1. Since the HP acts like a piston injecting fast-magnetosonic perturbations into the VLISM, it is not surprising that fastmode perturbations dominate the spectrum of fluctuations. While it is clear from our estimates summarized in Table 2 that the turbulent Mach number is small, the observed N-shaped profiles and intense gradients/directional discontinuities discussed in Section 3 suggest that wave steepening does occur and transverse modes are coupled to the compressible fluctuations (Medvedev 1999). In the range of frequencies of $10^{-8} \lesssim f \lesssim 10^{-6}$ Hz, this scenario is consistent with the coherent cascade, an archetypal example of which is the Burgers turbulence (Burgers 1995). This may also explain the $P \sim k^{-2}$ power law observed in the low-frequency regime. The heliospheric forcing makes turbulence in the VLISM different from that discussed in Cho & Lazarian (2002) (CL02), where compressible modes are drained from Alfvénic modes and constitute only a small fraction of fluctuations, which scales as the square of the turbulent Mach number. In that case, the Alfvénic cascade essentially follows the GS95 scaling and is unaffected by the fast-mode cascade.

Burlaga et al. (2018) extrapolated the observed VI spectra to estimate the upper limit for the outer scale of strong LISM turbulence, i.e., the scale where $\delta B_{\rm rms} = B_0$. This was done by using the Kolmogorov's 5/3 spectrum. Note that a similar extrapolation can be done easily using the second-order structure functions shown in Figure 10. In fact, assuming that the LISM turbulence is incompressible at the outer scale, a saturation of the turbulent cascade is expected when $\mathcal{I}_2 = 1/4\langle |\Delta \boldsymbol{B}|^2 \rangle /B_0^2 \approx 1$. Using the Kolmogorov's $\ell^{2/3}$ scaling for the second-order structure function one can

extrapolate the curves shown Figure 10 and calculate the outer scale as $\ell_{LISM} \approx \ell^*/\mathcal{I}_2(\ell^*)^{3/2}$, where * indicates a point selected in the observed inertial range. Using the data from Figure 10 (top panel) in interval I3, and choosing $\ell^* = 10^{10}$ m and $B_0 = 0.3$ nT, we arrive at $\ell_{LISM} \approx 0.02$ pc (0.01 pc, if the longitudinal fluctuations are also considered). If interval I1 is chosen, the estimate is $\ell_{LISM} \approx 0.035$ pc. This is similar of the previous estimate of 0.01 pc. However, we point out that, first, it is still debatable that the Kolmogorov scaling is appropriate. Intermittency corrections should be applied to the scaling law in \mathcal{I}_2 second, the previously discussed heliospheric forcing effect very likely makes such extrapolation meaningless. This is also suggested by the break of the statistics shown in Figure 10 on the largest scales considered therein and by significant differences in the scaling laws inside the five considered time intervals.

The range of intermediate/small frequencies, for $f \gtrsim$ 10^{-6} Hz, has been disregarded in the previous publications because of the uncertainty caused by the weakness of fluctuations and presence of data gaps. We have shown that in spite of the high noise level, physically meaningful fluctuations can be detected in this regime, occasionally showing intermittency, high correlation between different components of B, repeated patterns, and similarity with the profiles observed on large scales. On the intermediate scales, a spectral flattening occurs yielding the 1/f power laws at $f \gtrsim 10^{-6}$ Hz. While it is certainly possible that noise affects this regime, the recent identification (Fraternale et al. 2020) of enhanced microscale fluctuations and Kolmogorov-like scaling at $f^* \approx 10^{-4}$ Hz suggests that some physical processes contribute to the spectral broadening. In addition to shockrelated fluctuation enhancement, which starts abruptly on 2014.486 and is associated with S2, we have shown that similar small-scale features are also present in late 2018.

Of interest is the observed persistence of small-scale longitudinal fluctuations through the year of 2019. The magnetic compressibility is found to grow with increasing frequency, the maximum of ≈ 0.6 being reached at $f \approx 5 \times 10^{-4}$ Hz. A possible explanation of this phenomenon may be due the three-wave resonance analyzed by Zank et al. (2019) on the basis the nearly incompressible MHD theory. The conversion of fast modes into Alfvénic modes obtained from this theory was used by Zank et al. (2019) as an explanation for the presence of large-scale transverse fluctuations observed by V1 after 2015. However, the persistence of small-scale longitudinal fluctuations was not considered in details.

Besides Alfvénic modes produced in the interaction of fast modes, the production of slow modes is also admissible. If this actually occurred, generated slow modes would have a much larger wavenumber than the original mode. This might be an explanation of the spectral broadening of B_{\parallel} and steepening of the spectra occasionally observed at $f \gtrsim 10^{-4}$ Hz. Note that CL02 predict that slow-mode and entropy waves should follow the GS95 dynamics similarly to the Alfvén modes (see also Cho & Lazarian 2003; Eyink et al. 2011). However, other known wave—wave interaction processes also may be responsible for the increase in compressibility observed in the transitional, MHD-to-kinetic regime. This is known to occur in the SW turbulence (Alexandrova et al. 2013). It is worth noting that some of the observed microscale profiles resemble

shocklets, but we cannot ascertain their nature because of the lack of plasma data.

Another process expected to be present in the VLISM is the instability of PUI distributions and related self-generated magnetic fluctuations, or ion-cyclotron waves. The relevant scales may be detectable by V1, since they are in the range of $0.1 \lesssim kr_{ci} \lesssim 1$ (Roytershteyn et al. 2019). The rms intensity of B_{\perp} fluctuations in saturation continuous, as shown by Roytershteyn et al. (2019), may be $\langle \delta B_{\perp}^2 \rangle / B_0^2 \approx 8 \times 10^{-5}$ for realistic PUI densities and VLISM parameters (see Figure 4 in their paper). Figure 10 shows that small-scale fluctuations at VI are close to that level.

In spite of existing uncertainties and approximations made, the magnetic energy flux shown in Figure 9 is significantly larger than the value of 10^{-25} erg cm⁻³ s⁻¹ reported by Florinski et al. (2016). We have compared the observed flux to the rate of wave power generated by instability processes of the PUI distribution. According to Florinski et al. (2016), the latter rate is around 8×10^{-24} erg cm⁻³ s⁻¹. In Section 4.4, we obtained magnetic energy cascade rates in the range of 10^{-23} – 10^{-22} erg cm⁻³ s⁻¹. More specifically, the magnetic energy rate in the low-frequency range was lower than in the high-frequency range, which may indicate that different processes contribute to the observed turbulence, the PUIs instability being a candidate process in the high-frequency range close to the ion scale. Then, it would be worthwhile to compare the shape of the magnetic field structures observed by V1 to that arising from the PUI instability process in numerical simulations. In addition, since the scale of this turbulence overlaps with the gyroradius of $\sim 1-100 \,\mathrm{MeV}$ electrons, a possibility should be investigated that the properties of turbulence in this regime may be relevant to the observed isotropization of the flux of energetic electrons discussed by Rankin et al. (2020).

Finally, we recall that under the assumption that the collisional theory holds, a large separation exists between the kinematic viscosity and the magnetic diffusivity (i.e., large magnetic Prandtl number $Pr_m = D_\mu/D_\eta$). This condition may contribute to the spectral flattening observed for magnetic field fluctuations in the intermediate frequency range. In the viscosity-damped regime with $Pr_m \gg 1$ discussed by Cho & Lazarian (2003), magnetic field fluctuations on scales below the viscous dissipation scale are shown to have a 1/f power spectral distribution, very strong anisotropy, and scaling properties differing from the MHD turbulence. Further investigation should be carried out to understand the nature of the "effective" viscosity and resistivity in the VLISM and physical processes governing them.

This work is supported by NASA grants 80NSSC19K0260, 80NSSC18K1649, 80NSSC18K1212, and NSF-BSF grant PHY-2010450. The authors are grateful to Leonard F. Burlaga for invaluable discussions. We acknowledge the NASA Space Physics Data Facility (https://cohoweb.gsfc.nasa.gov/coho/).

Appendix A Coulomb-collision Frequencies and Transport Coefficients

Following (Chap. 4 in Zank 2014), we calculate the collision frequencies associated with the scattering process of a test particle a moving at velocity v_a through a background population of particles b assuming a Maxwellian distribution f_0 for the background field and thermalization at $T = T_e = T_p$.

The scattering frequency is given by

$$\nu_s^{ab}(v) = \frac{2n_b q_a^2 q_b^2 \ln \Lambda_{ab} m_b}{4\pi \epsilon_0^2 m_a^3 v_{th,a}^3} \left(1 + \frac{m_a}{m_b}\right) \frac{T_a}{T_b} \frac{G(v/v_{th,b})}{v/v_{th,a}}, \quad (A1)$$

$$G(x) = \frac{f(x) - xf'(x)}{2x^2}, \quad f = \text{erf}(x),$$
 (A2)

$$v_{th,j} = \left(\frac{2k_{\rm B}T_j}{m_j}\right)^{1/2} \quad j = a, b.$$
 (A3)

The frequencies shown in Table 1 are obtained by numerical integration giving us

$$\nu_s^{ab} = 4\pi \int_0^{\nu_{\text{max}}} d\nu \ \nu_s^{ab}(\nu) \nu^2 g_b(\nu), \tag{A4}$$

$$f_{0b}(v) = \left(\frac{m_b}{2\pi k_B T_b}\right)^{3/2} \exp\left[\frac{-m_b v^2}{2k_B T_b}\right],$$
 (A5)

where v is the random velocity (no drift motion). We choose $v_{\max} = 5 \ v_{th,b}$ and $\int_0^\infty dv \ 4\pi v^2 g(v) = 1$. Note that the collision frequencies given by Equation (A4)

Note that the collision frequencies given by Equation (A4) differ by the factor of \sim 5% from those obtained the formulae from Goedbloed & Poedts (2004) for both ion and electron frequencies:

$$\tau_{ee} = (\nu^{ee})^{-1} = 6\pi\sqrt{2\pi}\,\epsilon_0^2 \frac{\sqrt{m_e}\,(k_B T)^{3/2}}{e^4 n_e \ln(\Lambda)} \tag{A6}$$

$$\tau_{pp} = (\nu^{pp})^{-1} = 6\pi\sqrt{2\pi}\,\epsilon_0^2 \frac{\sqrt{m_p}\,(k_{\rm B}T)^{3/2}}{e^4 n_e \ln(\Lambda)}.\tag{A7}$$

In magnetized plasmas, the viscosity tensor can be expressed as a sum of five components (Braginskii 1965). We estimate the ion viscosity using the zeroth term (*parallel viscosity*), since the other terms are relatively smaller, being $(\omega_{cp}/\nu^{pp})^{-1} \approx 10^{-6}$ and $(\omega_{ce}/\nu^{ee})^{-1} \approx 10^{-8}$ (see also the discussion in Baranov & Ruderman 2013). The Braginskii parallel viscosity coefficients for p-p and e-e collisions are

$$\mu_0^p = 0.96 \ n_p k_{\rm B} T_p \tau^{pp}, \quad \mu_0^e = 0.73 \ n_e k_{\rm B} T_e \tau^{ee}.$$
 (A8)

The mean-free paths can be estimated as

$$\lambda^{pp} = \frac{v_{th,p}}{\nu^{pp}}, \quad \lambda^{ee} = \frac{v_{th,e}}{\nu^{ee}}.$$
 (A9)

The classical, perpendicular electric conductivity (Cohen et al. 1950), resistivity, and magnetic diffusivity are given by

$$\sigma_{\perp} = 2\sigma_{\parallel} = \frac{e^2 n_e}{m_e \nu^{ee}}, \quad \eta = \frac{1}{\sigma}, \quad D_{\eta} = \frac{1}{\mu_0 \sigma},$$
 (A10)

where $e=1.6022\times 10^{-19}$ C is the elementary charge, $\epsilon_0=8.8542\times 10^{-12}$ Fm⁻¹, $\mu_0=4\pi\times 10^{-7}$ Hm⁻¹ are the electric permittivity and magnetic permeability in vacuum, respectively; $m_e=9.109\times 10^{-31}$ kg is the electron mass.

The ion kinematic viscosity, ion thermal diffusivity, and the magnetic and Bohm diffusion coefficients are given by

$$\begin{split} D_{\mu} &= \frac{\mu^{p}}{n_{p} m_{p}}, \ D_{\eta} = \frac{1}{\mu_{0} \sigma}, \\ D_{th} &= \frac{\gamma - 1}{\gamma} \frac{k_{\parallel}^{p}}{n_{p} m_{p}}, \ D_{\text{Bohm}} = \frac{k_{\text{B}} T_{p}}{e B_{0}}, \end{split} \tag{A11}$$

where

$$k_{\parallel}^{\ p} = 3.9 \frac{n_p k_{\rm B} T_p \tau_{pp}}{m_p}$$
 (A12)

is the parallel thermal conductivity of ions.

Appendix B Statistical Convergence of High-order Structure Functions of Magnetic Field Increments

To determine the maximum order, q_{max} , for which a structure function can be meaningfully estimated, we used the procedure developed by Dudok de Wit (2004). The results are shown in Figure 11. As far as the fourth-order moments of magnetic field increments are concerned, the statistical convergence is ensured for all intervals and values of τ . The total numbers of data points in our high-resolution data sets are $N_{\text{tot}} = 262,168, 126,615, 179,412, 202,916, \text{ and } 136,248 \text{ for }$ intervals I1-I5, respectively. As shown with the black curves in the leftmost panels of Figure 11, the actual number of available increments, $N_i(\tau)$, naturally decreases with increasing τ , due to the finite size of the data set. Moreover, for the specific Voyager data sets, N_i reach minima at τ corresponding to the typical periodicity of the largest data gaps (8–12 hr), and starts to oscillate afterwards. At the minimum of N_i , the accuracy is lower, but still ensures convergence of the fourth-order structure function. It is worth noting that the structure functions are computed from the available increments, without any interpolation inside the gaps. Note also that I3 and I5 are the most critical intervals from the moments' convergence perspective.

In Figure 12, we provide an estimate of accuracy of the $q^{\rm th}$ -order structure functions computed from the data using a well-known relationship for the moments of order 2q (Tennekes & Lumley 1972; Podesta et al. 2009). For any generic quantity y, the rms relative error for an empirical moment $M_q = \langle y^q \rangle$ is

$$\epsilon_q = \left| \frac{\sigma}{\mu} \right|_{M} = \left| \frac{\alpha t_c}{t_f} \left(\frac{M_{2q}}{M_q} - 1 \right) \right|^{1/2},$$
 (B13)

where σ and μ are the standard deviation and the average of M_q , respectively, t_f is the length of a time series, and $t_c(\tau)$ is the correlation length of y^q . For correlated signals, e.g., the increments, the ratio of t_c/t_f is a substitute of the factor N^{-1} . For a more conservative estimate, we also introduce a factor $\alpha \approx 3$, which takes into account that $\sim 70\%$ of data is missing. Let us consider the increments $y(t; \tau) = \Delta_\tau B_R$ and show the results for interval I3.

Since the estimate of M_{2q} may be inaccurate, Podesta et al. (2009) suggested an alternative approach in order to estimate ϵ_q . In this approach, the data set is split into n_s subsamples with N_s data points in each of them, and M_q is computed for these subsamples separately. It is then possible to compute the average value and the variance of M_q , and therefore obtain $\epsilon_{q,s}(N_s)$. Repeating the process for different segmentations, e.g., by increasing n_s , an $\epsilon_{q,s} \sim 1/\sqrt{N_s}$ law is observed, and the power-law fit allows one to extrapolate ϵ to larger values of N_s . In particular, we extrapolate it to the total number of increments in the data set, $N_i(\tau)$.

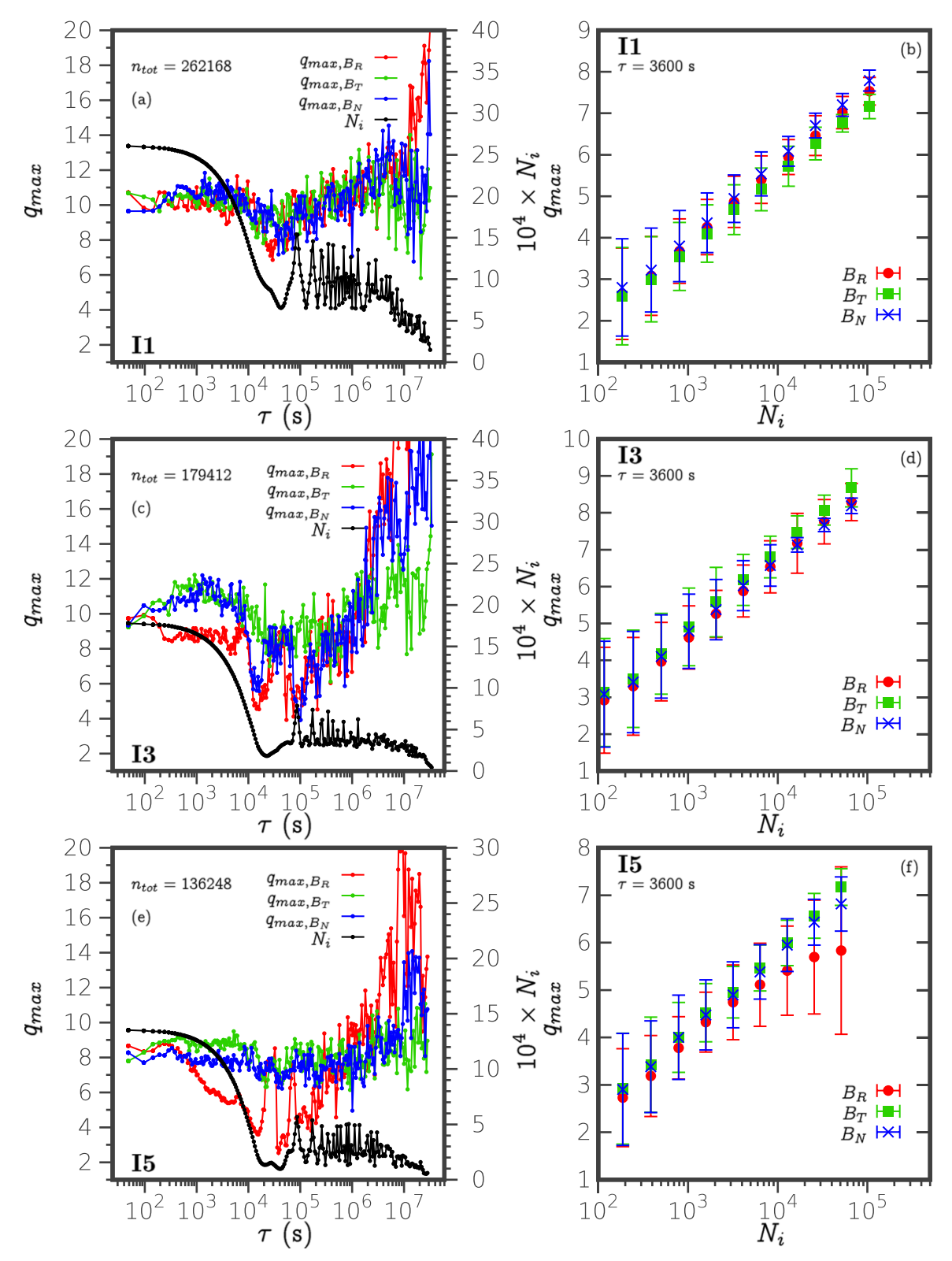


Figure 11. Convergence of the increment statistics for intervals I1, I3, and I5 (from the top to the bottom). Left panels: the maximum order of converging statistics, q_{max} , for the absolute moments $\langle |\Delta B_j(\tau)|^q \rangle$ as a function of time lag τ . On the right vertical axis we show the number of available increments, N_i , which is affected by both the finite sample size and the presence of data gaps. In particular, the minimum reached near $\tau = 20,000-40,000$ s and subsequent oscillations are due to the largest gaps of 8–12 hr length, which occur every day in the Voyager time series. Right panels: the average value and standard deviation of q_{max} are shown as a function of the increment number for $\tau = 3600$ s. This is done by splitting each interval into a series of non-overlapping subsamples.

When the increments are analyzed, as in our case, this process is sensitive to the choice of τ . Moreover, for Voyager data, certain combinations of τ and n_s , some subsamples may

have insufficient number of points, due to the presence of data gaps. In the left panel of Figure 12, we show the relative error for the second- and fourth-order structure functions of

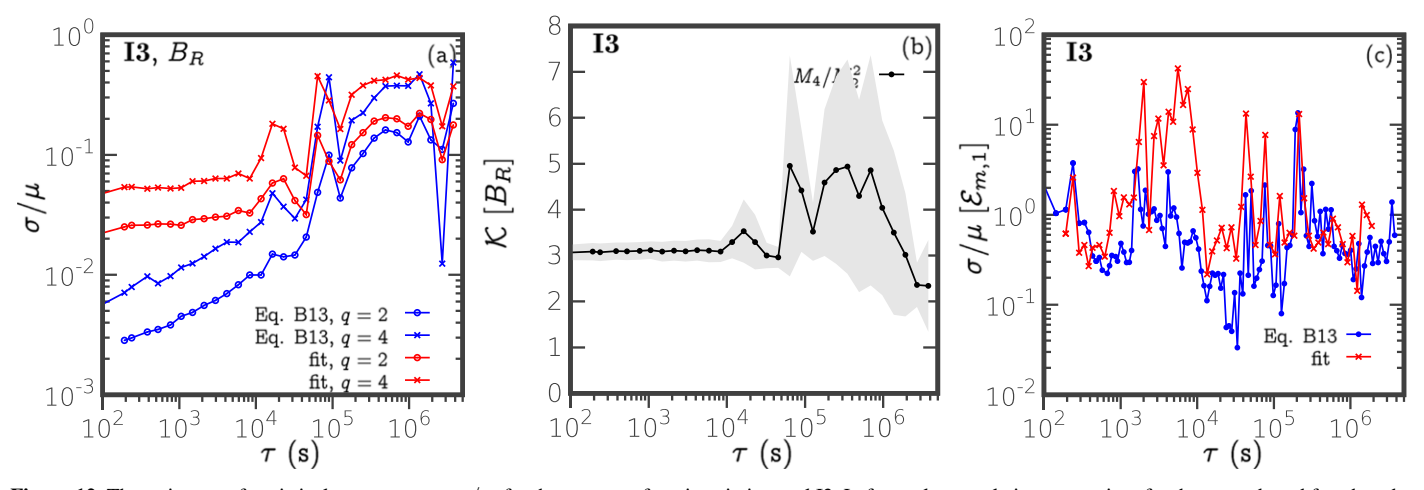


Figure 12. The estimates of statistical accuracy, $\epsilon = \sigma/\mu$, for the structure functions in interval I3. Left panel: rms relative uncertainty for the second- and fourth-order structure moments, estimated using Equation (B13) (blue curves) and with the fitting procedure described in the text, for 32 values of τ uniformly distributed in log space. Middle panel: the kurtosis of B_R is shown together with its uncertainty band shaded in gray. Right panel: rms relative uncertainty for the third-order moment $\mathcal{E}_{m,1}$ (Equation (11)).

 $B_R \approx B_{\perp 2}$ in interval I3. The results obtained with the procedure described above and those resulting from the application of Equation (B13) are compared. As expected, the statistical uncertainty grows with τ . The fitting procedure leads to larger errors. The maximum uncertainty is ≈ 0.5 for q=4 and $\tau\gtrsim 10^5$ s. We use these error estimates to derive the uncertainty in the calculation of the kurtosis (see the green curve in Figure 8(c)) shown in the middle panel of Figure 12. The upper and lower bounds of the shaded region are given by $\mathcal{K} \pm \sigma_{\mathcal{K}}$, with $\sigma_{\mathcal{K}} = \mathcal{K} [\epsilon_{M_4}^2 + \sqrt{2} \epsilon_{M_2}^2]^{1/2}$, representing a conservative estimate of the standard deviation of K. Peaks and oscillations of K (e.g., blue and green curves in Figure 8) are induced by data gaps, since they are in phase with the counter N_i , but the data gaps themselves do not generate intermittency, as have been verified by using a Gaussian synthetic turbulence data set.

As far as the signed, third-order moments are concerned (Equations (11) and (12)), a separate consideration of the positive and negative parts of the increment distribution (suggested by Dudok de Wit 2004) yields results similar to those shown in Figure 11, ensuring convergence of the statistics. However, it is well known that the accuracy of calculation of the odd moments is certainly lower than that of the even moments, especially when the mean values are very small. The relative error of the moment $\mathcal{E}_{m,1}$ (Equation (11)) for interval I3 is shown in the rightmost panel of Figure 12. Comparison with Figure 9 shows that relatively small values of σ/μ around 0.05–0.5 correspond to the largest absolute values of $\mathcal{E}_{m,1}$. By contrast, the maxima lying above the value of 1 in Figure 12 correspond to the smallest values of $\mathcal{E}_{m,1}$. Note that most of near-zero values have been filtered out from the data shown in Figure 9.

ORCID iDs

Federico Fraternale https://orcid.org/0000-0002-4700-2762 Nikolai V. Pogorelov https://orcid.org/0000-0002-6409-2392

References

Alexandrova, O., Chen, C. H. K., Sorriso-Valvo, L., Horbury, T. S., & Bale, S. D. 2013, SSRv, 178, 101
Bandyopadhyay, R., Sorriso-Valvo, L., Chasapis, A., et al. 2020, PhRvL, 124, 225101

```
Baranov, V. B., & Malama, Y. G. 1993, JGR, 98, 15157
Baranov, V. B., & Ruderman, M. S. 2013, MNRAS, 434, 3202
Berdichevsky, D. B. 2009, Voyager Mission, Detailed processing of weak
   magnetic fields; II - Update on the cleaning of Voyager magnetic field density
  B with MAGCALs, https://vgrmag.gsfc.nasa.gov/20151017BzPLestimates_
  wMAGCAL.pdf
Borovikov, S. N., Pogorelov, N. V., & Ebert, R. W. 2012, ApJ, 750, 42
Braginskii, S. I. 1965, in Reviews of Plasma Physics, ed. M. A. Leontovich
  (New York: Consultants Bureau)
Burgers, J. M. 1995, in Selected Papers of J. M. Burgers, ed.
  F. T. M. Nieuwstadt & J. A. Steketee (Berlin: Springer)
Burlaga, L., & Ness, N. 2011, JGRA, 116, A05102
Burlaga, L. F., Florinski, V., & Ness, N. F. 2015, ApJL, 804, 31
Burlaga, L. F., Florinski, V., & Ness, N. F. 2018, ApJ, 854, 20
Burlaga, L. F., & Ness, N. F. 2014, ApJL, 795, 19
Burlaga, L. F., & Ness, N. F. 2016, ApJ, 829, 134
Burlaga, L. F., Ness, N. F., Berdichevsky, D. B., et al. 2019, ApJ, 877, 31
Burlaga, L. F., Ness, N. F., Berdichevsky, D. B., et al. 2020a, AJ, 160, 40
Burlaga, L. F., Ness, N. F., Berdichevsky, D. B., et al. 2020b, ApJL, 901, L2
Burlaga, L. F., Ness, N. F., Gurnett, D. A., & Kurth, W. S. 2013, ApJL, 778, 3
Cairns, I., & Zank, G. P. 2002, GeoRL, 29, 1143
Cannon, B. E., Smith, C. W., Isenberg, P. A., et al. 2014, ApJ, 784, 150
Cho, J., & Lazarian, A. 2002, PhRvL, 88, 245001
Cho, J., & Lazarian, A. 2003, MNRAS, 345, 325
Coburn, J., Forman, M. A., Smith, C. W., et al. 2015, RSPTA, 373, 20140150
Cohen, R. S., Spitzer, L., Jr, & Routly, P. M. 1950, PhRv, 80, 230
Donoho, D. L. 2006, ITIT, 52, 1289
Dudok de Wit, T. 2004, PhRvE, 70, 055302
Eyink, G. L., Lazarian, A., & Vishniac, E. T. 2011, ApJ, 743, 51
Fahr, H. J., & Ripken, H. W. 1984, A&A, 139, 551
Fermo, R. L., Pogorelov, N. V., & Burlaga, L. F. 2015, JPhCS, 642, 012008
Florinski, V., Heerikhuisen, J., Niemiec, J., & Ernst, A. 2016, ApJ, 826, 197
Fraternale, F., Pogorelov, N. V., & Burlaga, L. 2020, ApJL, 897, L28
Fraternale, F., Pogorelov, N. V., Richardson, J. D., & Tordella, D. 2019a, ApJ,
Fraternale, F., Pogorelov, N. V., Richardson, J. D., & Tordella, D. 2019b,
   JPhCS, 1225, 012006
Frisch, U. 1995, Turbulence: The Legacy of AN Kolmogorov (Cambridge:
  Cambridge Univ. Press)
Gallana, L., Fraternale, F., Iovieno, M., et al. 2016, JGRA, 121, 3905
Galtier, S. 2008, PhRvE, 77, 015302
Goedbloed, J. P., & Poedts, S. 2004, Principles of Magnetohydrodynamics:
   With Applications to Laboratory and Astrophysical Plasmas (Cambridge:
  Cambridge Univ. Press)
Goldreich, P., & Sridhar, S. 1995, ApJ, 438, 763
Gurnett, D. A., & Kurth, W. S. 2019, NatAs, 3, 1024
Gurnett, D. A., Kurth, W. S., Allendorf, S. C., & Poynter, R. L. 1993, Sci,
  262, 199
Gurnett, D. A., Kurth, W. S., Burlaga, L. F., & Ness, N. F. 2013, Sci,
Gurnett, D. A., Kurth, W. S., Stone, E. C., et al. 2015, ApJ, 809, 121
```

```
Hadid, L. Z., Sahraoui, F., Galtier, S., & Huang, S. Y. 2018, PhRvL, 120,
Holzer, T. 1989, ARA&A, 27, 199
Iroshnikov, P. S. 1964, SvA, 7, 566
Killick, R., Fearnhead, P., & Eckley, I. A. 2012, J. American Statistical Assoc.,
   107, 1590
Kim, T. K., Pogorelov, N. V., & Burlaga, L. F. 2017, ApJL, 843, 32
Klein, K. G., Howes, G. G., TenBarge, J. M., et al. 2012, ApJ, 755, 159
Kolmogorov, A. N. 1941, DoSSR, 30, 301
Kolmogorov, A. N. 1962, JFM, 13, 82
Kovasznay, L. S. G. 1948, PhRv, 73, 1115
Kraichnan, R. H. 1965, Phys. Fluids, 8, 1385
Kulikovskiy, A., & Liubimov, G. 1965, Magnetohydrodynamics (Reading:
   Addison-Wesley)
Leamon, R. J., Smith, C. W., Ness, N. F., & Wong, H. K. 1999, JGR, 104,
   22331
Lele, S. K., & Larsson, J. 2009, JPhCS, 180, 012032
MacBride, B. T., Smith, C. W., & Forman, M. A. 2008, ApJ, 679, 1644
Malama, Y. G., Izmodenov, V. V., & Chalov, S. V. 2006, A&A, 445, 693
Matsukiyo, S., Noumi, T., Zank, G. P., Washimi, H., & Hada, T. 2019, ApJ,
   888, 11
Matthaeus, W. H., Dasso, S., Weygand, J. M., et al. 2005, PhRvL, 95, 231101
McKenzie, J. F., & Westphal, K. O. 1970, Phys. Fluids, 13, 630
Medvedev, M. 1999, PhPl, 6, 2191
Monin, A. S., & Yaglom, A. M. 1971, Statistical Fluid Mechanics, Vol. II
   (Cambridge, MA: MIT Press)
Montgomery, D., & Turner, L. 1981, Phys. Fluids., 24, 825
Mostafavi, P., & Zank, G. 2018, ApJL, 854, L15
Narita, Y. 2018, LRSP, 15, 2
Obukhov, A. M. 1962, JGR, 67, 3011
Podesta, J. J. 2008, JFM, 609, 171
Podesta, J. J., Forman, M. A., Smith, C. W., et al. 2009, NPGeo, 16, 99
Pogorelov, N. V. 1995, A&A, 297, 835
Pogorelov, N. V. 2000, Ap&SS, 274, 115
Pogorelov, N. V., Borovikov, S. N., Heerikhuisen, J., & Zhang, M. 2015,
   ApJL, 812, 6
Pogorelov, N. V., Fichtner, H., Czechowski, A., et al. 2017a, Space Sci. Rev.,
   212, 193
```

```
Pogorelov, N. V., Heerikhuisen, J., Roytershteyn, V., et al. 2017b, ApJ, 845, 9
Pogorelov, N. V., & Matsuda, T. 1998, JGR, 103, 237
Pogorelov, N. V., Suess, S. T., Borovikov, S. N., et al. 2013, ApJ, 772, 2
Politano, H., & Pouquet, A. 1998, PhRvE, 57, R21
Rankin, J. S., McComas, D. J., & Schwadron, N. A. 2020, ApJ, 895, 103
Rankin, J. S., Stone, E. C., Cummings, A. C., et al. 2019, ApJ, 873, 46
Richardson, J. D., Belcher, J. W., Garcia-Galindo, P., & Burlaga, L. F. 2019,
   NatAs. 3, 1019
Roberts, D. A., & Goldstein, M. L. 1987, JGR, 92, 10105
Roytershteyn, V., Pogorelov, N. V., & Heerikhuisen, J. 2019, ApJ, 881, 65
Sahraoui, F., Goldstein, M. L., Belmont, G., Canu, P., & Rezeau, L. 2010,
  PhRvL, 105, 131101
Saxena, R., Bale, S. D., & Horbury, T. S. 2005, PhPl, 12, 052904
Smith, C. W., Isenberg, P. A., Matthaeus, W. H., & Richardson., J. D. 2006,
  ApJ, 638, 508
Sorriso-Valvo, L., Carbone, V., Veltri, P., Consolini, G., & Bruno, R. 1999,
  Geophys. Res. Lett., 26, 1801
Sorriso-Valvo, L., Catapano, F., Retinò, A., et al. 2019, PhRvL, 122, 035102
Sorriso-Valvo, L., Marino, R., Carbone, V., et al. 2007, PhRvL, 99, 115001
Steinolfson, R. S. 1994, JGR, 99, 13307
Stone, E. C., Cummings, A. C., McDonald, F. B., et al. 2013, Sci, 341, 150
Taylor, G. I. 1938, Proc. R. Soc. Lond. A, 164, 476
Tennekes, H., & Lumley, J. L. 1972, A First Course in Turbulence
  (Cambridge, MA: MIT Press)
Washimi, H., Zank, G. P., Hu, Q., et al. 2011, MNRAS, 416, 1475
Weygand, J. M., Matthaeus, W. H., Dasso, S., et al. 2007, JGRA, 112, A10
Weygand, J. M., Matthaeus, W. H., Dasso, S., et al. 2009, JGRA, 114, A7
Whitham, G. B. 1974, Linear and Nonlinear Waves (New York: Wiley)
Zank, G. 2015, ARA&A, 53, 449
Zank, G. P. 2014, Tranport Processes in Space Physics and Astrophysics, Vol.
  877 (Berlin: Springer)
Zank, G. P., Du, S., & Hunana, P. 2017, ApJ, 842, 114
Zank, G. P., & Müller, H.-R. 2003, JGR, 108, 1240
Zank, G. P., Nakanotani, M., & Webb, G. M. 2019, ApJ, 887, 116
Zhang, M., Pogorelov, N. V., Zhang, Y., et al. 2020, ApJ, 889, 97
Zhao, L.-L., Adhikari, L., Zank, G. P., Hu, Q., & Feng, X. S. 2017, ApJ,
Zirnstein, E. J., Giacalone, J., Kumar, R., et al. 2020, ApJ, 888, 29
```